ATLAS NOTE

ATL-TILECAL-PUB-2009-XXX

May 28, 2009

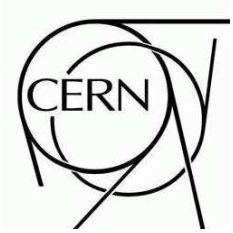

Study of the Response of the Hadronic Barrel Calorimeter in the ATLAS Combined Test-beam to Pions of Energies from 20 to 350 GeV for Beam Impact Points from 0.2 to 0.65

E. Khramov, V. Bednyakov, I. Budagov and N. Rusakovich, (JINR, Russia)
T. Carli and A. Henriques (CERN, Switzerland)
V. Giangiobbe (Dipartimento di Fisica INFN, Sezione di Pisa, Italy)
Z. Liang (Academia Sinica, Taiwan)
C. Santoni (Universite Blaise Pascal de Clermont-Ferrand II, France)
M. Simonyan (LAPP-Laboratoire d'Annecy-le-Vieux de Physique des Particules, France)

ATL-TILECAL-PUB-2009-007
04 June 2009

Abstract

A fully instrumented slice of the ATLAS detector was exposed to test beams from the SPS (Super Proton Synchrotron) at CERN in 2004. The results of the measurements of the response of the hadronic Tile calorimeter to pions with energy in the range 20 to 350 GeV that only shower in the Tile calorimeter are reported. The linearity and the resolution of the calorimeter were determined and compared to previous results and to the predictions of a simulation program using the toolkit Geant4.

Contents

Introduction

In the year 2004 an ATLAS combined test beam (CTB) program was carried out at CERN. A slice of the ATLAS detector composed of the final versions of all central sub-detectors was exposed to pion beams. The layout of the sub-detectors was designed to be as close as possible to the ATLAS layout. The Data Acquisition system (DAQ) [1] was also similar to the one being used in ATLAS.

The calorimeter system in ATLAS will be used to measure the energy of jets over a wide energy range from about 20 GeV to more than 1 TeV. In the central detector part (barrel), the calorimeter system consists of an electromagnetic calorimeter, using liquid argon as active medium and lead as absorber, and a hadronic calorimeter, using plastic scintillator as active medium and iron as absorber.

In this paper, a measurement of the response of the barrel hadronic calorimeter TileCal to pion beams with energies in the range 20 to 350 GeV is presented. The response was studied for various incident angles corresponding to pseudo-rapidities of $\eta_{beam} = 0.20, 0.25, 0.35, 0.45, 0.55$ and 0.65.

Particular care was given to the selection of clean pion samples starting showering in TileCal and to correcting for the fraction of the shower energy that escapes the detection (leakage effects). The measured pion responses were compared to the predictions of a Monte Carlo simulation program [2].

The results are compared to previous measurements where the TileCal alone was exposed to test-beams.

1 The Experimental Set-up

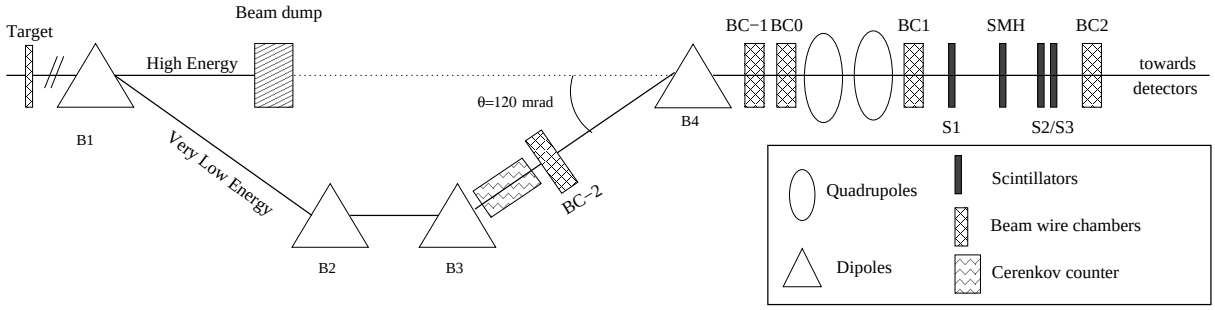

Figure 1: Schematic layout (not to scale) of the H8 beam line. Only the devices used during the data-taking are shown.

1.1 The Beam-line

The beams were produced by extracting 400 GeV protons from the Super Proton Synchrotron (SPS) machine. The primary target made of beryllium, had a length of 300 mm. The produced secondary beams can have energies from 10 to 350 GeV. A secondary filter target of 1000 mm of polyethylene plus an absorber of lead can be placed in the beam to produce tertiary beams. Bending magnets were used to determine the beam momentum and charge. The beams are expected to be composed mainly of pions and, in the case of positive beams, protons. Electrons and muons are also present. The results reported in this paper were obtained using positive beams with energies equal to 20, 50 and 100 GeV. Higher energy beams (150, 180, 200, 250, 320 and 350 GeV) had a negative charge. Positive beams of 150 and 180 GeV were also used.

Figure 1 shows the instrumentation of the beam line upstream of the detectors. The transverse beam profile is monitored by four wire chambers (BC-1 to BC2) [3]. Two scintillators (S2/S3), with an active surface of 5×5 cm^2, were used in coincidence to trigger the data acquisition (Physics trigger) and to provide the trigger timing. These two detectors together with the scintillator S1 were used to reject beam particles interacting upstream the detectors. In this paper we will use a right-handed coordinate system with the *x*-axis along the beam line and the *y*-axis pointing up.

More details can be found in ref. [4].

1.2 The Detector

Figure 2 shows a side-view of the layout of the ATLAS sub-detectors during the 2004 CTB. Only sub-detectors that were used in the present analysis are shown. The ATLAS inner detector [5] consists of three systems: the Silicon Pixel Detector, the Semiconductor Tracker (SCT) and the Transition Radiation Tracker (TRT). During the data taking period analysed here the inner detector system was not operational. It has been used in a later data taking period, where it was fully operational, for the determination of the proton contamination.

The electromagnetic calorimeter (LAr) consisted of one module of the Liquid Argon calorimeter [6] placed inside a cryostat made of aluminium. The beam entrance and exit walls were each $\lambda = 0.1$ interaction lengths thick. The calorimeter has four longitudinal layers, including a pre-sampler. The coverage of all four layers is $0 < \eta < 1.4$ and -$\pi/16 < \phi < \pi/16$ rad (see Fig. 2 and Fig. 3 for η and ϕ orientation convention). The $\eta - \phi$ granularity of each longitudinal layer is given in Table 1 and described in more detail in ref. [6].

The hadronic calorimeter was composed of three modules of the scintillating tiles calorimeter (TileCal) [7]. The TileCal modules were placed about 30 cm behind the LAr calorimeter.

The total coverage of the sub-detector was $-1 < \eta < 1$ and $-1.5 < \phi < 1.5$. Each TileCal module has three longitudinal layers, whose $\eta - \phi$ granularity is described in ref. [7] (see also Fig. 3). A sketch of the calorimeter lay-out and the cell granularity is shown in Fig. 3. The beam impact points are indicated as lines.

LAr and TileCal were both supported by a mobile table. This table was oriented in such a way that the incoming particles in the calorimeters were projective in pseudo-rapidity as in the ATLAS experiment.

The cryostat scintillator (SC1) situated between the LAr cryostat and the TileCal modules (see Fig. 2 and Fig. 3) was used to remove pions that started showering in the cryostat exit wall. Such a scintillation counter is not present in the ATLAS detector. The distance between the LAr and the TileCal was 30 cm. This is a bit longer than the 25 cm in the ATLAS detector (see Table 1). Another scintillation counter (SMT) was placed behind the table and an absorber, to identify muons belonging to the beams.

Various sections of the ATLAS muon spectrometer [8] were also present in the 2004 CTB set-up. This sub-detector has not been used for the analysis presented in this paper.

1.3 Measurement of the Beam Energies

The beam energy is calculated for each run from the magnet currents and the beam-line collimator settings. This method relies on work done for the LAr calorimeter in the 2002 test-beam analysis [9], where a system of Hall probes was used to precisely determine the magnetic field in the bending magnets.

Based on this Hall probe measurement the relation between the measured magnet currents and the magnetic field in the bending magnets is known. The precision of the knowledge of the beam momenta has been calculated using:

$$\frac{\Delta E_{\text{beam}}}{E_{\text{beam}}} = \frac{25\%}{p} \oplus 0.5\%, \tag{1}$$

where p is the beam momentum. The measured beam momenta are given in Table 26.

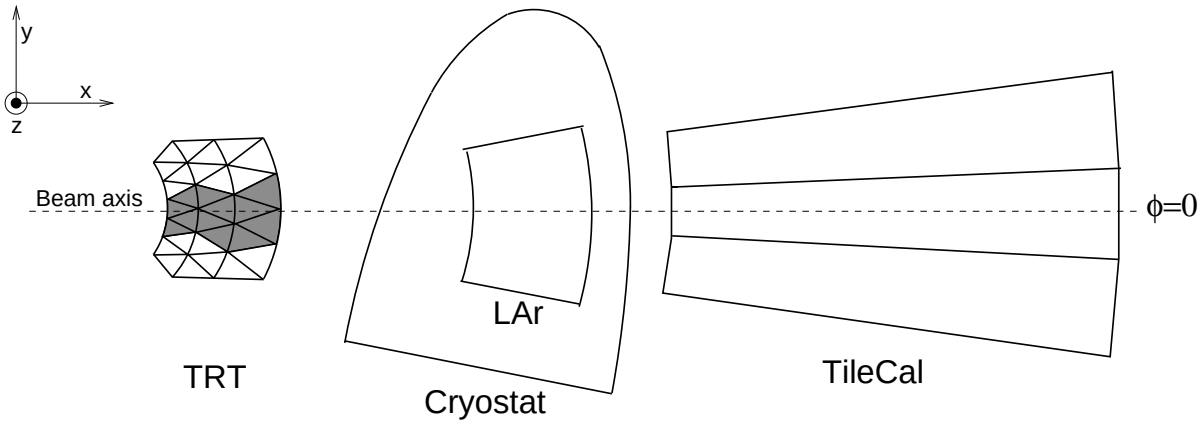

Figure 2: Side view of the detector layout in the 2004 combined test beam. Only sub-detectors that are used in this paper are represented

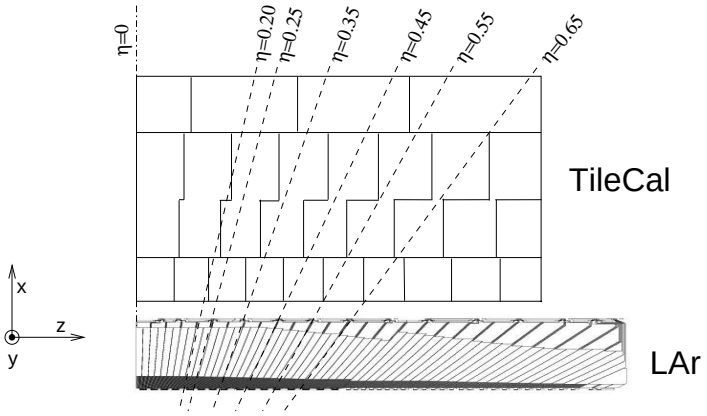

Figure 3: View of the calorimetry layout in the 2004 Combined Test Beam. The top part of the figure represents the Tile calorimeter, the bottom part the Lar calorimeter. The solid lines give the cell granularity. The dotted lines inidicate the pseudo-rapidity intervals at which a particles impinges on the calorimeter, if is has its origin in the proton–proton interaction point. The TileCal modules are only represented for $\eta > 0$.

	Layers granularity	CTB 2004	ATLAS
LAr	$\Delta\eta \times \Delta\phi = 0.0031 \times 0.1$ $\Delta\eta \times \Delta\phi = 0.025 \times 0.0245$ $\Delta\eta \times \Delta\phi = 0.05 \times 0.025$	Thickness at $\eta = 0$: $6+16+2 = 24X_0$ $(\equiv 1.2\lambda)$	Thickness at $\eta = 0$: $6+16+2 = 24X_0$ $(\equiv 1.2\lambda)$
Cryostat		$\approx 1X_0$	$\approx 1X_0$
Distance between LAr and TileCal		≈ 30 cm	≈ 25 cm
TileCal	$\Delta\eta \times \Delta\phi = 0.1 \times 0.1$ $\Delta\eta \times \Delta\phi = 0.1 \times 0.1$ $\Delta\eta \times \Delta\phi = 0.2 \times 0.1$	Coverage in ϕ: 0.294 rad (3 modules) Thickness at $\eta = 0$: $1.4+4.0+1.8 = 7.2\lambda$	Coverage in ϕ: 2π rad (64 modules) Thickness at $\eta = 0$: $1.4+4.0+1.8 = 7.2\lambda$
Active thickness		$\approx 9.2\lambda$ at $\eta = 0$	$\approx 9.2\lambda$ at $\eta = 0$

Table 1: Characteristics of the configuration of the LAr and Tile calorimeters in the CTB 2004 set-up and in the ATLAS detector.

2 Reconstruction of the Calorimeter Energy

2.1 Cell Energy Reconstruction

2.1.1 LAr calorimeter

The electronic calibration of the LAr calorimeter in the CTB is described in detail in ref. [10].

The cell energy is reconstructed from the measured cell signal using:

$$E_{\mathrm{rec}}^{\mathrm{cell}} = F_{\mu A\rightarrow \mathrm{MeV}} \cdot F_{DAQ\rightarrow\mu A} \cdot \frac{1}{\frac{M_{\mathrm{phys}}}{M_{\mathrm{cali}}}} \cdot \sum_{i=1,2} R_i \left[\sum_{j=1}^{N} \mathrm{OFC}_j \left(S_j - P\right) \right]^i . \tag{2}$$

The pedestal level, P, can be determined from dedicated calibration runs with no beam or using random triggers during the data taking of physics events.

The factor R_i relates the amplitude to a well known electronic pulse (in DAC-counts). It is obtained by calibration runs where the injected current is changed in small steps ("ramp run"). A higher order polynomial to relate the reconstructed amplitude and the injected charge is used. The factor $F_{DAQ\rightarrow\mu A}$ relates the setting of the electronic calibration system to the current injected to the electronics. The amplitude (A) of the sampled signal (measured in the ADC-counts) is reconstructed using a digital filtering technique [11], where the peak amplitude is expanded in a linear weighted sum of coefficients (OFC) and the pedestal (P) is subtracted in each sample.

The LAr electromagnetic energy scale was determined comparing the measured and simulated energy response of 180 GeV electrons. The uncertainty on the scale, due mainly to uncertainty in the knowledge of the beam momentum is 0.7% [10].

2.1.2 Tile calorimeter

The charge injection system (CIS) calibrates the response of the read-out electronics and a radioactive caesium source (Cs) is used to equalize the PMT-gains and to set the electromagnetic scale.

The scintillating light produced in the tiles is transported via wavelength shifting fibres into photomultipliers (PMT). The PMTs amplify the signal and convert the optical signal into an electrical one. Each PMT channel has two analogue paths: the high and the low gain with 82 cts/pC and 1.3 cts/pC, respectively. The read-out electronics shapes, amplifies and digitises the signals from the PMTs. The shaped signals are sampled every 25 ns by a 10-bit ADC.

The measured channel energy is reconstructed by:

$$E_{\mathrm{rec}}^{\mathrm{chan}}[\mathrm{pC}] = F_{\mathrm{ADC}\rightarrow\mathrm{pC}} \cdot F_{Cs} \cdot \left(A_{\mathrm{fit}} - P_{\mathrm{fit}}\right), \tag{3}$$

where A_{fit} corresponds to the peak height of the pulse after baseling subtraction, the factor $F_{\mathrm{pC}\rightarrow\mathrm{ADC}}$ is the electronic calibration factor measured with the CIS system [12], F_{Cs} corrects for cell non-uniformities using the caesium calibration system. The cell energy is reconstructed as the sum over the two channels each read-out by one PMT.

The electronics calibration of the TileCal is described in more detail in ref. [13].

2.2 Electromagnetic Scale and Uncertainties in the TileCal

The signal calibrated with the CIS- and the Cs-system is converted to an absolute energy using a calibration factor ($e = F_{\mathrm{pC}\rightarrow\mathrm{MeV}}$) that is obtained using electrons. This calibration factor defines the electromagnetic scale.

The response of the TileCal cells of about 10% of the TileCal modules installed in the ATLAS detector has been studied using electron test-beams in 2002 and 2003 [14]. The average response of

highly energetic electrons impinging at a polar angle of 20^o on the TileCal divided by the beam energy is defined as the $F_{\mathrm{pC}\rightarrow\mathrm{MeV}}$ calibration factor[1)]. It is measured to be $F_{\mathrm{pC}\rightarrow\mathrm{MeV}} = 1.050 \pm 0.003$ pC/GeV. The cell response variation is $2.4 \pm 0.1\%$ [13, 14].

The dominant part of the residual cell non-uniformity of about 2% for electrons is due to differences in the optical properties of the tiles and the read-out fibres (intra-cell) [2)].

The resulting rms spread of the pion response is $1.5 \pm 0.4\%$ [13]. This spread includes the cell-to-cell and the module-to-module variation. The cell-to-cell pion response variation within one module is about $0.6 - 0.7\%$. It is mainly due to tile-to-tile differences estimated to be 0.5% and due to the uncertainty in the CIS calibration that contributes with 0.42%.

After Cs-equalization there is still underlying systematics that is different for each of the three TileCal compartements that is corrected using measurements with muons impinging on the calorimeter side [14].

Since the electromagnetic scale has been determined using the A-cell, in this analysis this cell is used as the reference and the response in the BC-cells and D-cells is changed by 0.977 and 0.919, respectively.

2.3 The Electronic Noise, Hot and dead cells

For each run, the standard deviation σ_{noise} of the electronic noise has been determined for each PMT of the calorimeter using randomly triggered events. Typical σ_{noise} values are 12 MeV (1st layer of LAr), 28 MeV (2nd layer of LAr), 22 MeV (3rd layer of LAr), 30 MeV (1st layer of TileCal), 30 MeV (2nd layer of TileCal) and 25 MeV (3rd layer of TileCal). The total expected standard deviation of the electronic noise is $\simeq 100$ MeV. This value is negligible with respect to the energies reconstructed in the calorimeter and has a negligible effect on the pion energy resolution.

No hot and dead channels were identified in the Tile calorimeter during the data taking.

2.4 Pion Energy Reconstruction

The reconstructed shower energy E_{rec} in the TileCal calorimeter was obtained as the sum of the energy deposited in all the PMTs of the calorimeter having $\eta_{\mathrm{cell}} > 0$. No corrections for dead material effects or for the compensation of nuclear effects were applied.

In order to improve the energy resolution, only cells with energy E_{cell} larger than twice the standard deviation of the electronic noise σ_{noise} (in absolute value) were considered in the sum:

$$|E_{\mathrm{cell}}| > 2 \times \sigma_{\mathrm{noise}}. \tag{4}$$

3 Monte Carlo Simulation

3.1 Modelling of Particle Interactions with the Detector Material

The experimental results were compared to the predictions of the Monte Carlo (MC) simulation program Geant4 [3)] [2].

The Monte Carlo simulation models the interaction of particles with the detector material on a microscopic level. The detailed shower development follows all particles that interact electromagnetically in the calorimeter with an expected travel path (range) larger than 1 mm. Besides purely electromagnetic

[1)] Due to the varying size of the tiles and the iron absorber as a function of the particle impact point, the electrons response varies by about 10% between small angles $\eta = 0$ and large angle $\eta = 0.65$ [13, 14].

[2)] Such differences can be determined by the *Cs*-calibration system, but not corrected for, since the smallest read-out entity is a cell and the particle impact on the cell is not known a-priori.

[3)] The version 4.91 has been used.

processes, also hadron interactions and photo-nuclear interactions are simulated. Neutrons are followed in detail up to 10 μsec. After that time all their energy is deposited at the location of the neutron.

The strong interaction of hadrons is modelled in four phase depending on the energy range:

1. the interaction of the projectile with the nucleus using parameterised reaction cross-section for various processes (fission, capture, elastic, inelastic scattering)

2. the fragmentation of the partons produced in the inelastic hadron nucleon collision using theory driven or parameterised models ($\approx$ 10 GeV - 10 TeV)

3. The interactions of the hadrons in the medium of the nucleus are modelled using intra-nuclear nucleon cascades ($1-10$ GeV).

4. Nuclear processes to de-excite or split the excited nucleus via spallation, break-up, fission etc.($1-100$ MeV).

The QGSP_BERT hadronic showering model was used in the simulation. This is the model presently being used in the simulation of the ATLAS detector for proton proton collisions.

The interaction of the projectile particle with momenta above 25 GeV with the nucleus is modelled using the quark-gluon string model [15–19] that describes hadron-nucleus interactions by selecting the collision partners from the nucleus, splitting the nucleon into quarks and di-quarks and by forming and fragmenting excited strings.

In the momentum range below about 10 GeV the Bertini nuclear cascade [20–22] is used that describes the intra-nuclear hadronic interactions of hadrons and de-excites the residual nucleus.

In the moment range in between 10-25 GeV the Low Energy Parametrised (LEP) is used that uses parameterisations of measured particle spectra and multiplicities for the simulation of the hadron showers.

The QGS (LEP) model is always used for energies above 25 GeV (below 12 GeV). Hadrons between 12 and 25 GeV are treated by either model, with the choice being made event by event by a linearly varying probability.

3.2 Modelling of the Detector Response

In the simulation the detector material and geometry were fully described.

The simulation of the TileCal scintillators includes saturation effects modelled according to Birks law [23–25] and the effects of photo-statistics in the photo-multipliers. However, no attempt is made to describe the detailed optical properties of the scintillating tiles and the read-out fibres.

Also the details of the light attenuation between the two PMTs is not modelled. A simple model of the energy sharing between 2 PMTs using a linear approximation is used to distribute the energy to the PMT on each cell side. The maximal drop of the signal between the two PMTs of a cell due to non-linearities is not larger than 5%.

The electronic noise was extracted from experimental data using randomly triggered events and added incoherently to the energy of each PMT in the MC samples. Coherent noise is not simulated, but known to be relatively small [26].

The mean and spread of the incoming pion beam momentum correspond to what was measured. The spatial and angular distributions of the beam were also tuned to reproduce the experimental ones [4)].

A total of 10k-20k events were simulated for each beam energy and impact position. The amount of experimental data is smaller by approximately one order of magnitude.

[4)] The spatial distribution of the beam was measured using the beam chambers BC1 and BC2 (see Fig 1).

4 Data-set and Event Selection

4.1 Data-Set

The data have been taken from end of August to middle of September 2004. The inner detector was not operational during this data taking period, but was present in the beam-line.

Many analyzed data at various beam impact points between $0.2 \leq \eta \leq 0.65$ and beam energies between $20 \leq E_{\text{beam}} \leq 350$ GeV have been recorded. The run-numbers used for each beam impact point and for each beam energy are summarised in Table 26.

For some of the runs negatively charged pions and for others positively charged pions have been used. For beam energy at 150 and 180 GeV both pion charges are available. The pion electrical charge of the beam particles is indicated in Table 26 by the sign in front of the pion energy.

4.2 Event Selection

Each beam chamber *BCn* (n = 1, 2 and 3) allows a determination of the beam profiles in the transversal axis y and z: y_{BCn} and z_{BCn}. The means (μ_{BCn_y} and μ_{BCn_z}) and the widths of the distributions correspond to the root mean squared (rms) of the measured beam impact point distribution. The σ values are about 30 mm and are determined run–by–run.

The accepted events have the impact point coordinates verifying in each chamber n the conditions (cut 5):

$$\begin{aligned} \mu_{BCn_y} - 2\,\text{rms}_{BCn_y} < y_{BCn} < \mu_{BCn_y} + 2\,\text{rms}_{BCn_y} \\ \mu_{BCn_z} - 2\,\text{rms}_{BCn_z} < z_{BCn} < \mu_{BCn_z} + 2\,\text{rms}_{BCn_z}. \end{aligned} \tag{5}$$

The divergence of the beam was estimated using the differences of the impact points coordinates in the chambers BC0, BC1 and BC1, BC2, respectively:

$$\begin{aligned} \Delta y_{0,1} &= y_{BC0} - y_{BC1}, \\ \Delta y_{1,2} &= y_{BC1} - y_{BC2}, \\ \Delta z_{0,1} &= z_{BC0} - z_{BC1}, \\ \Delta z_{1,2} &= z_{BC1} - z_{BC2}. \end{aligned}$$

The retained events have to verify the conditions (cut 6):

$$\begin{aligned} \mu_{y_{0,1}} - 2\sigma_{y_{0,1}} < \Delta_{y_{0,1}} < \mu_{y_{0,1}} + 2\sigma_{y_{0,1}} \\ \mu_{y_{1,2}} - 2\sigma_{y_{1,2}} < \Delta_{y_{1,2}} < \mu_{y_{1,2}} + 2\sigma_{y_{1,2}} \\ \mu_{z_{0,1}} - 2\sigma_{z_{0,1}} < \Delta_{z_{0,1}} < \mu_{z_{0,1}} + 2\sigma_{z_{0,1}} \\ \mu_{z_{1,2}} - 2\sigma_{z_{1,2}} < \Delta_{z_{1,2}} < \mu_{z_{1,2}} + 2\sigma_{z_{1,2}}. \end{aligned} \tag{6}$$

The symbols μ and σ indicate the mean values and the sigmas of Gaussian functions fitting the difference distributions.

At the considered energies electrons impinging in the calorimeter deposit essentially all their energy in the LAr. In the case of pions, a large fraction of the energy is deposited in TileCal. Electrons were then rejected requiring (cut 7):

$$\frac{E_{\text{LAr}}}{E_{\text{LAr}} + E_{\text{TileCal}}} < 0.98. \tag{7}$$

Here, E_{LAr} denotes the energy measured in the LAr calorimeter and E_{TileCal} denotes the energy measured in TileCal (see also section 2).

Muons events were rejected allowing only noise in the SMT (cut 8):

$$E_{\mathrm{SMT}} < 500\ [\mathrm{ADC\ counts}]\ . \tag{8}$$

The mean energy deposited in the calorimeter by muons is much smaller than the one deposited by pions. A further rejection was obtained requiring (cut 9):

$$E_{\mathrm{LAr}} + E_{\mathrm{TileCal}} > 0.3\, E_{\mathrm{beam}}, \tag{9}$$

where E_{beam} is the beam energy.

The cuts on the beam line scintillator signals applied to reject events produced by beam particles interacting upstream of the detector or by double particles were established studying the responses of $S1$, $S2$ and $S3$ to muons. The following cuts were applied to select only events with one particle impinging on the calorimeter (cut 10):

$$\begin{aligned} E_{\mathrm{S1}} &< \mu_{\mathrm{S1}} + 2\,(\mu_{\mathrm{S1}} - \mu_{\mathrm{S1,noise}}) \\ E_{\mathrm{S2}} &< \mu_{\mathrm{S2}} + 2\,(\mu_{\mathrm{S2}} - \mu_{\mathrm{S2,noise}}) \\ E_{\mathrm{S3right}} &< \mu_{\mathrm{S3right}} + 2\,(\mu_{\mathrm{S3right}} - \mu_{\mathrm{S3right,noise}}) \\ E_{\mathrm{S3left}} &< \mu_{\mathrm{S3left}} + 2\,(\mu_{\mathrm{S3left}} - \mu_{\mathrm{S3left,noise}}) \end{aligned} \tag{10}$$

The μ and σ are, respectively, the mean values and the rms obtained from the signal distributions of selected muons or random triggers. The scintillator $S3$ was read by two photo-multipliers indicated as "left" and "right" in the equation 10.

4.3 Selection of Pion Showering only in TileCal

To select pions that do not strongly interact before reaching TileCal, a small energy deposit was required in the LAr calorimeter. For each of the three layers of the LAr calorimeter the cell with the maximum deposited energy ($\mathrm{cell_{max}}$) and its neighbour with the maximum energy ($\mathrm{cell_{nei}}$) were identified in the region $\eta_{\mathrm{beam}} - 0.2 < \eta < \eta_{\mathrm{beam}} + 0.2$, where η_{beam} is the pseudo-rapidity value of the nominal beam impact point. If the conditions (cut 11):

$$E_{\mathrm{cell_{max},i}} + E_{\mathrm{cell_{nei},i}} < \mu_{\mathrm{LAr,i}} + 2\sigma_{\mathrm{LAr,i}} \tag{11}$$

is fulfilled for each layer i the event is retained. The quantities $\mu_{\mathrm{LAr}}(i)$ and $\sigma_{\mathrm{LAr}}(i)$ are the mean values and the rms of the corresponding distributions obtained using muon events selected by requiring a signal in the SMT counter.. These cuts will, of course, remove further any electron contamination in the samples.

The events produced by pions showering in the cryostat exit wall were rejected using the SC1 scintillator. The signal distribution obtained in the case of a negative 180 GeV beam at $\eta = 0.35$ is shown in Fig. 8a and Fig. 8b. They show the SC1 signal distribution obtained for selected muons and for events collected by opening randomly the acquisition between the beam bursts. The muon signal is compatible with a particle traversing the scintillator as a minimum ionising particle.

The following cut on the energy deposited in SC1, E_{SC1}, was applied (cut 12):

$$E_{\mathrm{SC1}} < \mu_{\mathrm{SC1}} + N \times (\mu_{\mathrm{SC1}} - \mu_{\mathrm{noise}}), \tag{12}$$

where μ_{SC1} is the mean value of the distribution obtained using muons for each E_{beam}, N is an adjustable cut value for which the default is set to $N = 2$ and μ_{noise} is the mean value of the SC1 signal distribution obtained using random trigger events. Since the high voltage of the scintillator was changed for the

	η					
E_{beam} (GeV)	0.20	0.25	0.35	0.45	0.55	0.65
20	992	1150	834	671	853	660
50	1264	856	957	1418	876	870
100	–	1305	601	1917	1081	923
150	709	2617	1215	1384	544	700
-150	920	1410	1276	1048	399	–
180	951	1754	1512	1861	387	502
-180	1613	1143	1114	1565	170	899
-200	1778	1283	–	1920	459	942
-250	3946	1641	–	–	–	845
-320	962	1466	545	432	–	380
-350	1982	3471	594	–	–	–

Table 2: Number of events passing all selection criteria for the various nominal beam energies E_{beam} and beam impact points η. For some beam settings the SC1-scintillator was not available or the number of selected events was so low that no measurement was possible. The sign in front of the beam energy indicates the electrical charge of the beam particle.

various run μ_{SC1} and μ_{noise} are determined for each set of runs corresponding to one beam energy and one beam impact point.

The number of selected events varies between about 200 and 3500. The exact numbers are reported in Table 2 for all beam settings. For some beam settings the number of selected events was so low that no meaningful measurement was possible. Only runs where the SC1 scintillator was working are used in the analysis.

5 Energy Losses in the Dead material and by Leakage Calculated from Monte Carlo Simulations

Fig. 4a shows the fraction of the energy lost in the dead material with respect to the beam energy. For high pion energies $E > 100$ GeV the fractional energy losses are almost constant from $\eta = 0.25$ to $\eta = 0.65$, while for low pion energies the energy lost in the dead material increases from about 4% to 6% towards increasing η. A significant part (about 70-80%) of the energy lost in the dead material before the TileCal is due to the dead material in between the LAr and Tile calorimeters.

The energy loss in the dead material is about 5.5% at $\eta = 0.2$, while according to the behaviour of the energy loss as a function of the η at the same beam energy, the energy loss at $\eta = 0.20$ should be approximately $3.5-4$% (see Fig. 4a). These increased energy loss in the dead material are caused by six steel supporting rings of the LAr calorimeter. These rings are placed at $\eta = 0.20$, 0.40, 0.60 etc. and have a thickness of about $8-10$ cm. Fig. 4b shows the energy loss in the dead material when the supporting steel rings are removed from the test-beam geometry description. It can be seen that at $\eta = 0.20$ the energy loss in the dead material is about 3.7%.

The energy lost downstream of the calorimeter due to the longitudinal leakage decreases towards increasing η (see Fig. 4c), since the calorimeter becomes longer. The energy increase is approximately linearly proportional to the increase of the calorimeter length. For high pion energies the leakage decreases by about a factor of two, while for low pion energies the leakage decreases by 5%.

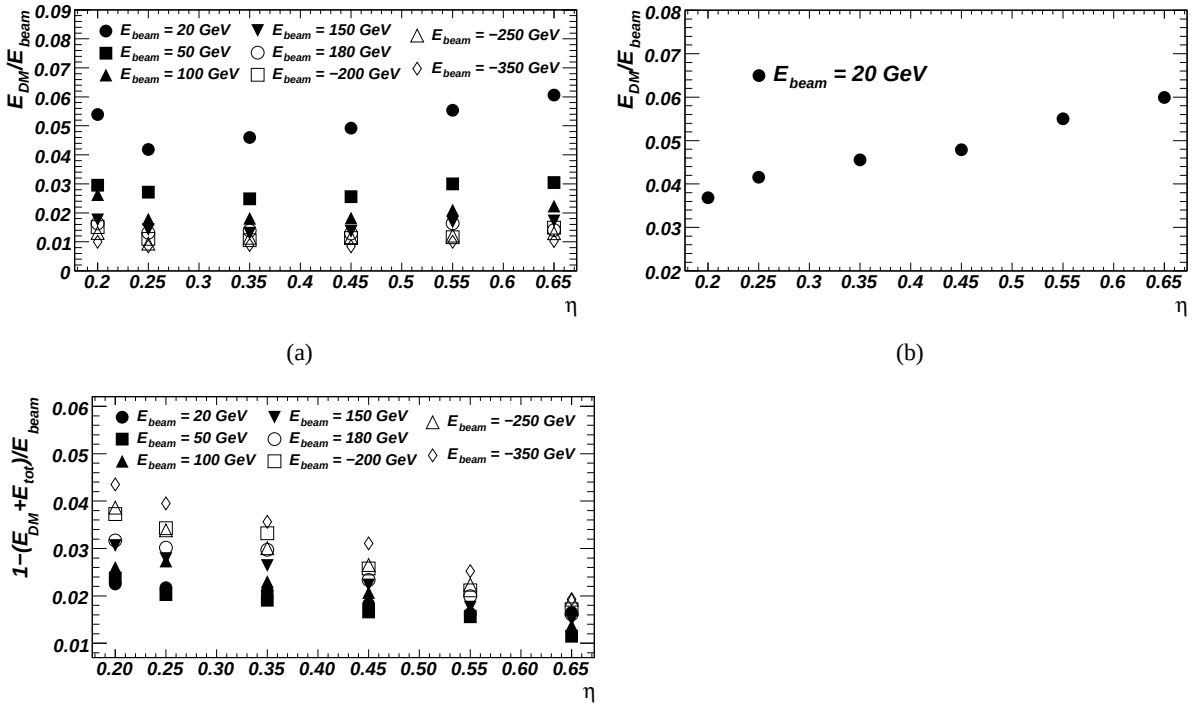

Figure 4: Fraction of the energy lost in the dead material before the TileCal and for the default set-up (a) and without the LAr support structure (b) as a function of the beam impact point for various beam energies. Energy lost downstream of the calorimeter (longitudinal leakage), calculated as the true energy deposited in the dead material before and in between the calorimeter and the energy deposited in the calorimeter, as a function of η for various beam energies (c). The requirements to select pions that do not shower before the TileCal are applied.

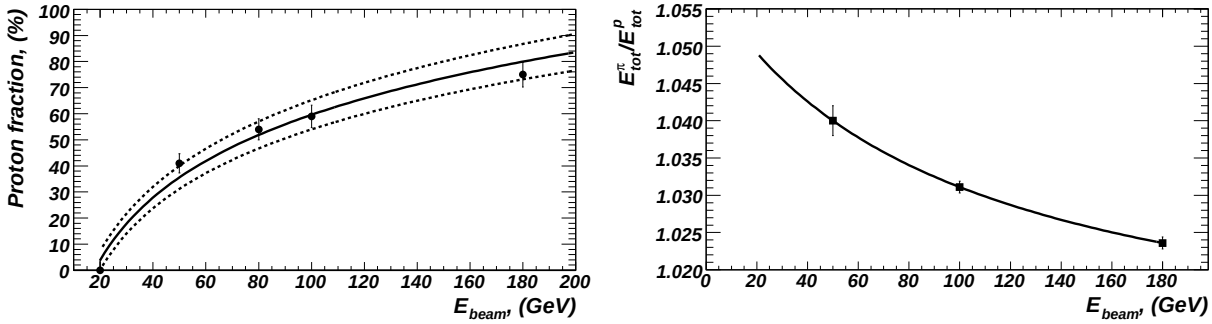

(a) (b)

Figure 5: a) Proton fraction in the pion beam as a function of beam energy as measured by the TRT in the CTB 2004 parametrised as in eq. 14. Only statistical errors are shown. The central value is shown as solid line, the statistical uncertainty as dashed lines. b) The ratio of the mean energy of pions and protons measured in the TileCal 2002 test-beam as a function of the beam energy. Overlayed as a solid line is the parameterisaton based on eq. 13 used in the correction for proton contamination. Only statistical uncertainties are shown;

6 Correction to the Pion Response and Resolution

6.1 Measurement of the Proton Contamination

The selected samples contain events produced by pions and, in the case of positive beams, protons. The TRT was designed to identify electrons that emit a large amount of transition radiation (TR) due to their high Lorentz γ-factor. On a statistical basis this feature can also be used to separate pions from protons, since pions begin to emit TR above beam momenta of about 30 GeV, which is not the case for protons (until 300 GeV).

Using a test-beam sample of identified muons and electrons at various beam momenta the shape of the higher threshold (HT) probability P_{HT} as a function of the Lorentz γ-factor can be measured [27].

Using an appropriate parameterisation of P_{HT}, the expected HT probability can be calculated for pions P^{π}_{HT} and for protons P^{p}_{HT}. By comparing P^{π}_{HT} and P^{p}_{HT} with the measured $P^{\mathrm{meas}}_{\mathrm{HT}}$ in a given run the fraction of protons in the pion beam is then determined. The obtained values are shown in Fig. 5a as a function of the beam energy.

6.2 Proton contamination Correction for Response and Resolution

The electromagnetic energy fraction in proton induced showers is lower than in pion showers by about 25% [28]. This will influence the measured response to pions and protons, since a non-compensated calorimeter has different response to electromagnetic *e* and hadronic *h* energy.

Since in the test-beam set-up no detector was installed that is able to discriminate pions from protons on an event-by-event basis, measurement of the mean pion and proton fraction in the hadron beam are used.

Differences between the response of pions and protons have been measured previously [28,29]. Here, the results from ref. [28] are used to parameterise the response ratio obtained for 50, 100 and 180 GeV pions and protons as:

$$R^{\pi/p}(E_{\mathrm{beam}}) = A/(E_{\mathrm{beam}} - B) + C. \tag{13}$$

The free parameters are adjusted to the data and are determined to be $A = 5.01$, $B = -94.66$ GeV and $C = 1.01$. The response ratio together with this parameterisation is shown in Fig. 5b. The numerical

	Beam energy (GeV)				
	20	50	100	150	180
f_p (%)	3.85	35.58	59.59	73.63	79.94
$R^{\pi/p} = E^{\pi}_{tot}/E^{p}_{tot}$	1.051	1.04	1.031	1.026	1.024
$1/k_p$	1.002	1.014	1.018	1.019	1.019
$R^{\pi/p}_{\sigma} = \sigma^{\pi}_{tot}/\sigma^{p}_{tot}$	1.084	1.114	1.142	1.161	1.169
$1/k^{\sigma}_{p}$	1.002	1.019	1.039	1.055	1.063

	Beam energy (GeV)				
	20	50	100	150	180
Δf_p, (%)	3.6	4.4	5.6	6.4	6.8
$\Delta E^{\pi}_{\rm tot}/E^{p}_{\rm tot})$	0.057	0.042	0.030	0.024	0.022
Δk_p	0.0026	0.014	0.017	0.017	0.017
$\Delta(\sigma^{\pi}_{\rm tot}/\sigma^{p}_{\rm tot})$	0.040	0.039	0.038	0.036	0.036
Δk^{σ}_{p}	0.0015	0.006	0.009	0.011	0.012

Table 3: Summary of the proton fraction f_p in the π^+ beam as obtained from a TRT measurement, the pion to proton response ratio $E^{\pi}_{\rm tot}/E^{p}_{\rm tot}$ as measured in the 2002 TileCal test-beam, the pion to proton resolution ratio $\sigma^{\pi}_{\rm tot}/\sigma^{p}_{\rm tot}$ and the final proton contamination correction factors for the response k_p and for the resolution k^{σ}_{p}. In the bottom part the uncertainties are quoted.

values of the response ratio are given in Table 3.

The dependence of the proton fraction for various beam momenta measured with the TRT during the CTB 2004 data taking period is parametrised using a logarithmic function

$$f_p = A_1 \cdot \log_{10}(B_1 \cdot E_{beam}). \tag{14}$$

The free parameters are adjusted to the data. They are determined to be $A_1 = 0.8$ and $B_1 = 0.056$. The TRT measurements together with this parameterisation are shown in Fig. 5a. The numerical values are summarised in Table 3.

The fraction of pions and protons in the beam can be written as $f_p + f_\pi = 1$. The distribution of the energy reconstructed in the TileCal should be a mixture of the distributions of the energy deposited by pions (E_π) and by protons (E_p):

$$< f(E_{rec}) >= N\left((1-f_p)\cdot e^{-\frac{(E_{\rm rec}-E_\pi)^2}{2\cdot\sigma^2_\pi}} + f_p \cdot e^{-\frac{(E_{\rm rec}-E_p)^2}{2\cdot\sigma^2_p}}\right), \tag{15}$$

where σ_π and σ_p are the width of the energy distribution for pions and protons and N is a normalisation factor.

To first linear approximation the mean reconstructed energy can be written as:

$$f(E_{rec}) = (1-f_p)\cdot E_\pi + f_p \cdot E_p. \tag{16}$$

The correction factor for the pion response can then be derived as:

$$k_p = \frac{E_{rec}}{E_\pi}, \text{ where } \mathrm{k_p} = (1-\mathrm{f_p}(\mathrm{E_{beam}})) + \mathrm{f_p}(\mathrm{E_{beam}})/\mathrm{R}^{\pi/\mathrm{p}}(\mathrm{E_{beam}}). \tag{17}$$

The correction factors obtained using eq. 17 for the pion response are given in Table 3. The correction is negligable for 20 GeV and decreases with increasing beam energy to about 2% at 180 GeV[5)]. The effect of the proton correction on the response at $\eta = 0.35$ as a function of beam momenta and for $E_{\text{beam}} = 180$ GeV as a function of η can be seen in Fig. 6a and Fig. 6b.

Before the correction for proton contamination at each beam impact point η the TileCal response to beams with positively charged particles is systematically lower than the response to beams with negatively charged particles. This can be seen for beam energies of 150 and 180 GeV, where beams with both charges are available in Fig. 6b). After the correction the ratio of the positively to negatively charged beam is in better agreement. The residual discrepancy is about 1%.

Thus, in further analysis data for π^- beam will be used at $E_{beam} = 150$ and 180 GeV. For lower beam energies a correction for proton contamination will be applied. A systematic uncertainty of 1% is assigned to the correction procedure.

The resolution of the calorimeter is also better for protons than for pions, since the fluctuations of the electromagnetic energy fraction is higher for pions than for protons. The resolution differences become smaller for increasing beam energies. The resolution measured for pions and protons in the 2002 test-beam as a function of beam energy is fitted by:

$$\sigma/E = a/\sqrt{E} \oplus b. \tag{18}$$

The correction for proton contamination is then calculated as:

$$k_p^\sigma = \frac{\sigma_{\text{rec}}}{\sigma_\pi}, \text{ with } k_p^\sigma = \sqrt{(1 - f_p(E_{beam})) + f_p(E_{beam})/R_\sigma^{\pi/p}(E_{beam})}, \tag{19}$$

where $R_\sigma^{\pi/p}$ is the ratio of the pion and the proton resolution as measured in the 2002 test-beam.

The obtained correction factors for the resolution are presented in Table 3. The correction is negligible at 20 GeV and then increases to 6% at 180 GeV. The effect of the correcting the resolution at $\eta = 0.35$ as a function of beam energy and at $E_{\text{beam}} = 180$ GeV as a function of the beam impact point is shown in Fig. 7c and Fig. 7d. The resolution of positively charged beams after correction of proton contamination corresponds to the resolution measured in negatively charged beams within a few percent.

6.3 Effect of the Cryostat Scintillator Selection Criterion on the Pion Response

To be able to compare to previous test-beam results, where only the TileCal has been exposed to pion beams, events have to be selected where the pions do not strongly interact before entering the TileCal. Besides the requirement of little energy deposited in the LAr calorimeter this can be achieved by requiring an energy deposit compatible with a minimally ionising particle (MIP) in the cryostat scintillator (SC1). The selection of such events has been discussed in section 4.3. Here, the possible biases on the pion response due to the event selection is discussed. This will allow to compare the results from the CTB to result where there was only little material in front of TileCal is discussed.

The SC1 signal distributions (in ADC counts) obtained in noise events and for events where a muon with energy of 180 GeV has been required, are shown in Fig. 8b. To take the varying experimental conditions into account the selection cut is based on the signal that is produced by a muon. The muon signal can be taken as a good representation for a pion that only interacts electromagnetically.

The cut value in SC1 is defined as follows:

$$\text{SC1}_{\text{cut}} = \mu_{\text{MIP}} + N_{\text{MIP}} \cdot \Delta\mu, \tag{20}$$

[5)] The comparison of correction factors obtained with eq.15 and its linear approximation at $\eta = 0.35$ shows a negligible difference of about 0.5%.

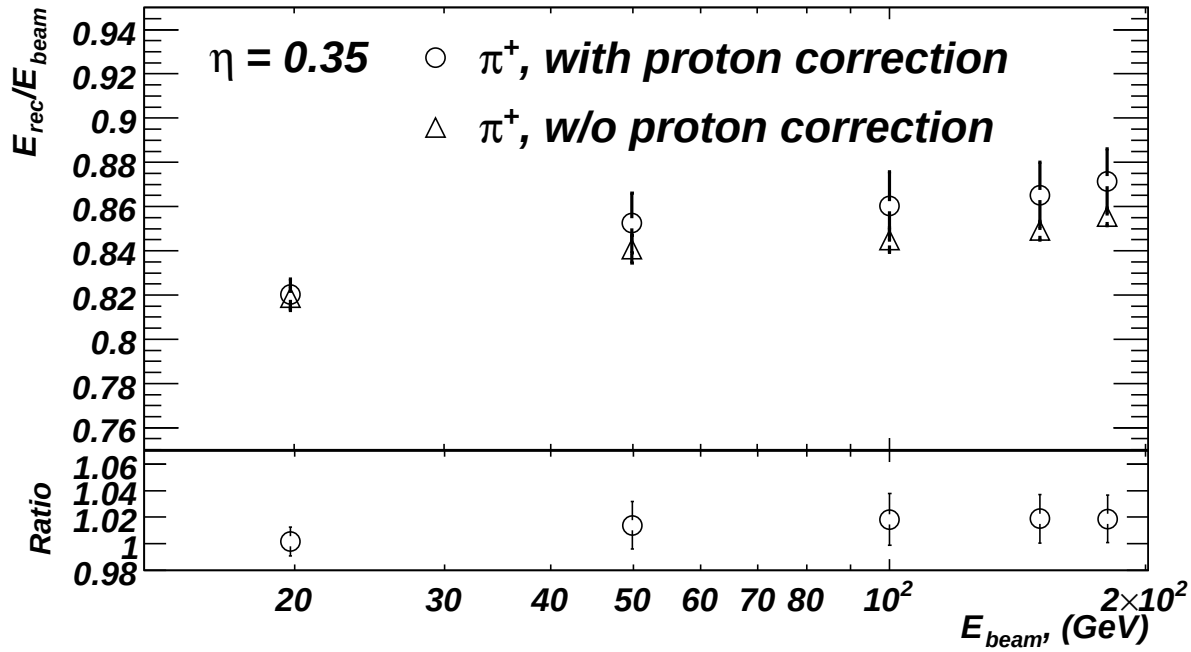

(a)

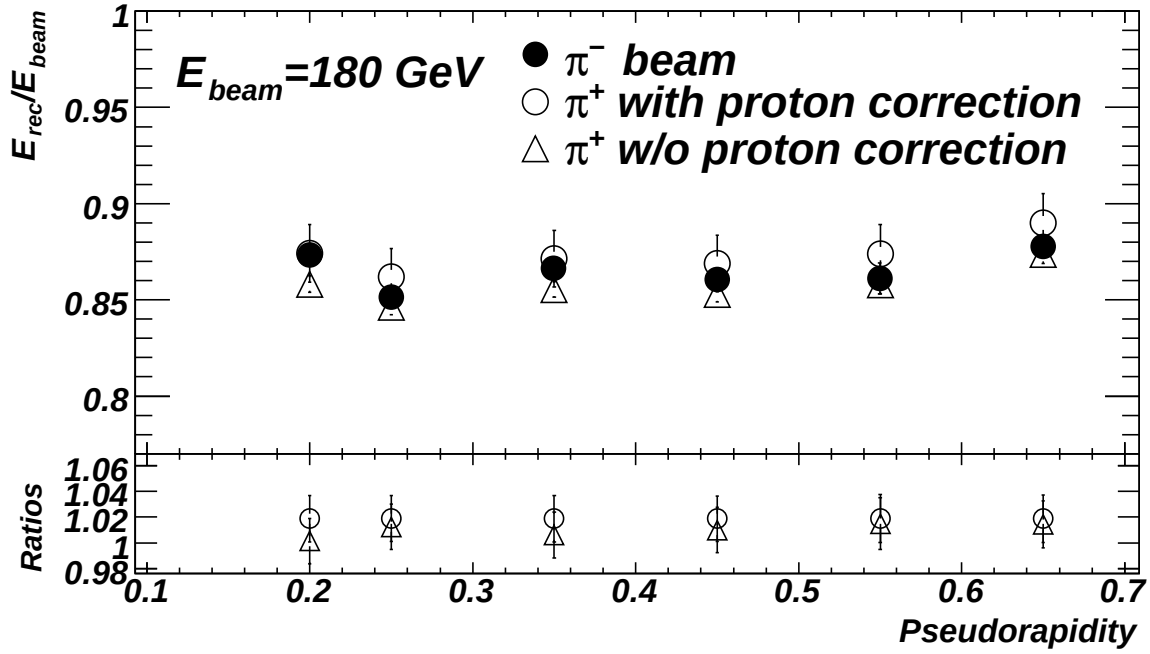

(b)

Figure 6: Fractional pion response with and without a correction for proton contamination as a function of the beam energy at $\eta = 0.35$ (a) and as a function of the beam impact point at $E_{\text{beam}} = 180$ GeV (b). The systematic uncertainty from the proton contamination correction is included. In the bottom part of the figure the ratio of the corrected response in the positively charged beam to the response in the negatively charged beam is shown as open triangles. The ratio of the response with and without the correction for positively charged beams is shown as open circles.

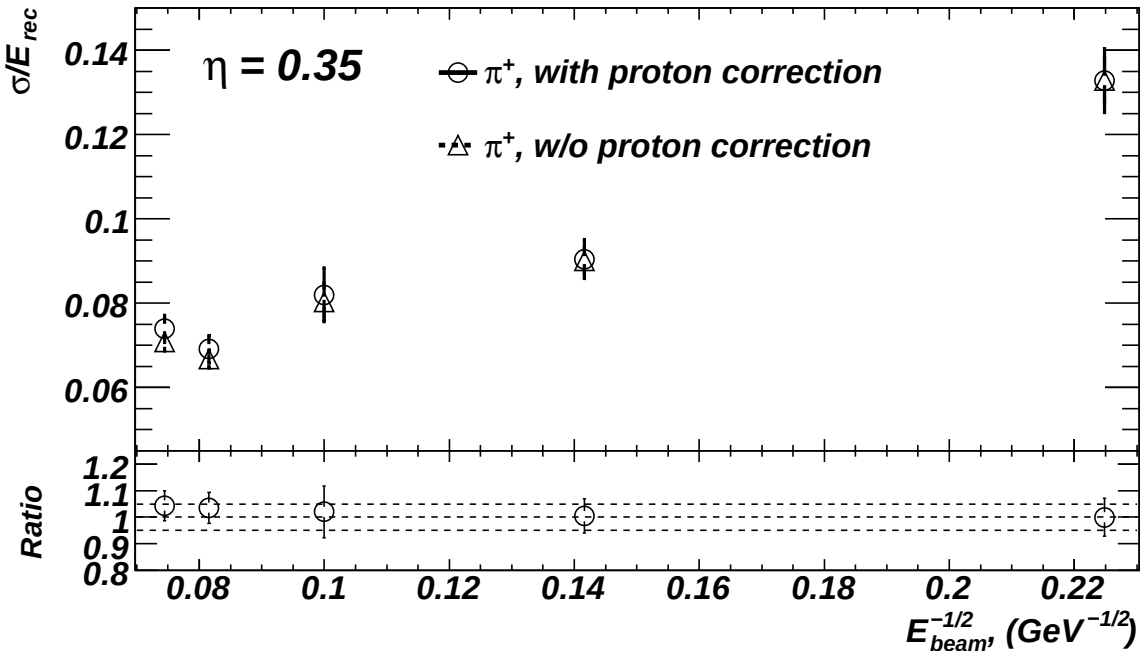

(a)

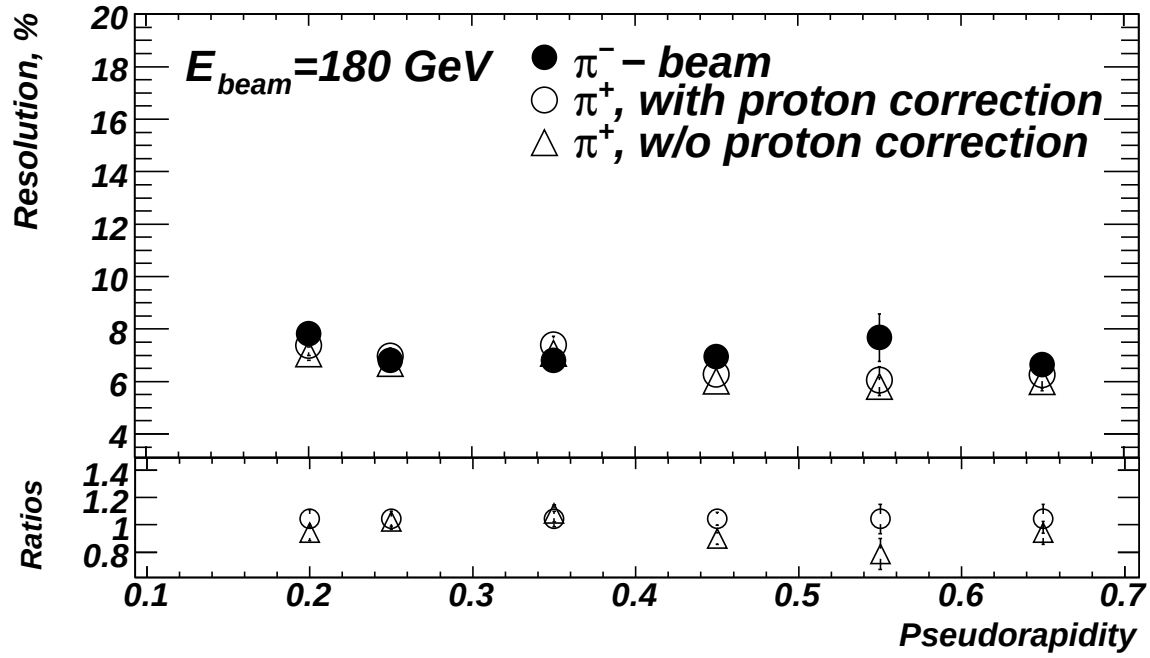

(b)

Figure 7: Fractional pion resolution (c,d) with and without a correction for proton contamination as a function of the beam energy at $\eta = 0.35$ (a) and as a function of the beam impact point at $E_{\rm beam} = 180$ GeV (b). The systematic uncertainty from the proton contamination correction is included. In the bottom part of the figure the ratio of the corrected response in the positively charged beam to the response in the negatively charged beam is shown as open triangles. The ratio of the response with and without the correction for positively charged beams is shown as open circles.

where μ_{MIP} is the mean value of the distribution measured for muons in SC1, N_{MIP} is the equivalent number of MIPs defined as $\Delta\mu = \mu_{\text{MIP}} - \mu_{\text{noise}}$, where μ_{noise} is the mean value of the noise distribution.

The cryostat scintillator was not implemented in the description of the test-beam set-up in the Monte Carlo simulation. However, the energy lost in the dead material, particularly between the LAr and the Tile calorimeters (DM) is known in the simulation. The energy corresponds to the total true deposited energy including energy deposits in nuclear reactions.

Fig. 8c and Fig. 8d shows the shape of the distribution of the energy loss in the dead material for simulated pions. As the distribution in the cryostat scintillator as measured for pions in the data this distribution has also a higher peak at low values corresponding to events where on minimally ionising particles passes and smaller peak that is caused by events that develop a hadron shower well before the Tile calorimeter.

Fig. 8d shows the low signal region using an enlarged scale. An equivalent of eq. 20 can be used in the simulation to reject pion events that start showering in the dead material between the LAr and the Tile calorimeters. In this way the effect of a cut on the dead material energy deposit can be studied.

By requiring small signals in SC1 pions showering before TileCal can be efficiently suppressed. However, there are also side effects due to back-scattering of particle produced in the hadronic shower that have to be considered. The SC1 selection requirement can influence the pion response via three main effects:

- **Energy losses in the dead material before TileCal**: Hadronic showers starting in between the LAr and Tile calorimeters (for a sketch see Fig. 9a and Fig. 9b) loose part of their energy in the dead material before the TileCal. Their response is therefore lower. These events have to be suppressed.

- **Response bias due to back-scattering**: Particles that are produced by a hadronic shower in the first layer of TileCal can be back-scattered and increase the SC1 signal (for a sketch see Figs. 9 a, b, c). The SC1 cut can then reject events with high hadronic activity where a lot of neutrons are produced. This might cause a lower pion response.

- **Changed longitudinal leakage due to back-scattering**: Since the back-scattered particles are at low energies, the probability that they leave a signal in the SC1 decreases when the shower starts later in the TileCal. Therefore a SC1 cut effectively decreases the TileCal length (for a sketch see Fig. 9 c, d), since hadronic showers starting close to the beginning of TileCal are suppressed. The response decreases and the resolution increases.

The effect of the SC1 cut on the response and the resolution depends on the pion energy. Dead material losses are most important for low pion energies. The effect of the lower response due to the production of a larger hadronic activity is rather small and only plays some role for low pion energies. This has been investigated using a Monte Carlo simulation. The change of the longitudinal leakage is only important for high pion energies.

The relevance of the three effects can be systematically investigated by varying the SC1 cut and studying the response and resolution at various beam energy and beam impact points. From these studies a systematic uncertainty on the biases introduced by the SC1 can be deduced.

When increasing the SC1 cut, events with more backscattering are more likely to be accepted and this causes the relative fraction of the energy lost downstream of the calorimeter to decrease. Since the calorimeter length is effectively longer the response increases and the resolution decreases. This effect should be largest at low η. For low beam energies where the downstream losses are not so important, however, an increasing SC1 cut decreases the response in TileCal and increases the resolution, since for such events the fluctuations in the energy lost in in front of the Tile calorimeter are larger.

Energy	20 GeV		320 GeV	
η	0.25	0.65	0.25	0.65
Linearity				
Data	-2.5%	-2.5%	$+0.5\%$	-0.2%
MC	-2.0%	-3.0%	$+0.8\%$	-1.7%
Resolution				
Data	$+7\%$	$+10\%$	-10%	-8%
MC	$+3\%$	$+12\%$	-12%	-10%

Table 4: Changes with and without the SC1 cut to the pion response and resolution. The sign indicates the change with and without the cut.

To verify this hypothesis the SC1 cut in the data or the cut on the energy lost in the dead material in the Monte Carlo simulation (DM) is systematically varied from $N = 0.5$ to $N = 14.5$ in steps of 0.5. Pions with an energy of 20 GeV and 350 GeV at $\eta = 0.25$, $\eta = 0.45$ and $\eta = 0.65$ requiring minimally ionisation energy loss in the LAr calorimeter are used to illustrate the effect of the SC1 cut. The results are shown in Fig. 10 and Fig. 11.

For low pion energies the response increases the stricter the cut on SC1 is. The effect is about 2.5% and 3% in test-beam data and Monte Carlo simulation, correspondingly. As it can be seen in Fig. 10 (top) in the data the response is similar for a strict SC1 cut for all η. When no SC1 cut is applied the results at $\eta = 0.25$ and $\eta = 0.65$ are similar, while the response at $\eta = 0.45$ is higher. Instead the simulation shows that the response decreases towards high η as expected from the increasing amount of dead material.

For high pion energies at $\eta = 0.25$ the response increases by 0.5% and 0.8% for test-beam and Monte Carlo simulation, correspondingly, when the MIP in SC1 (DM) cut is removed (see Figs. 11). At $\eta = 0.45$ the response is almost independent of the MIP in SC1 (DM) value, since the relative energy lost in the dead material and the longitudinal leakage are both small and compensate each other. At $\eta = 0.65$ the increased energy loss in the dead material is more significant than the decrease of the longitudinal leakage thanks to the increased calorimeter length. The effect of the SC1 cut on the pion response and resolution is summarised in Table 4.

At low energy the response increases, if the SC1 cut is applied, by $2-3\%$. The response increase does not depend on the length of the calorimeter. The Monte Carlo simulation describes the data. The resolution improves in the data by 7% for $\eta = 0.25$ to 10% at $\eta = 0.65$. The Monte Carlo simulation describes this behaviour at high η, but predicts a smaller resolution increase at low η (3%).

This behaviour is consistent with a reduction of the dead material losses due to the SC1 cut. the dead material losses are relatively large at low pion energies and seem to strongly influence the resolution.

At high pion energy the response decreases for low η and increases for large η, if the SC1 cut is applied. The Monte Carlo simulation gives a stronger dependence on the SC1 cut than found in the data. The resolution increases by 8% at high η and 10% low η.

This points to an effective shorting of the calorimeter length by the SC1 cut. The shortening of the calorimeter does influence less the resolution at high η and more at low η. For large η the response behaviour shows the same influence as for low energy. The dead material losses compensate the effective calorimeter shortening.

The effect of the cut on the cryostat scintillator can also be studied at the mean energy measured in the TileCal compartments. As it is shown in Fig. 12 for events with large signals in the cryostat scintillator about $3-4$ times more energy is deposited in the first layer, and about 1.5 lower in the second layer. This means that the events with a large SC1 signal start showering before the calorimeter and imposing a small SC1 signal can suppress the early showering pions. However, the longitudinal shower development also indicates that more energy leaks out when small signals in SC1 are required. Similar effects are seen

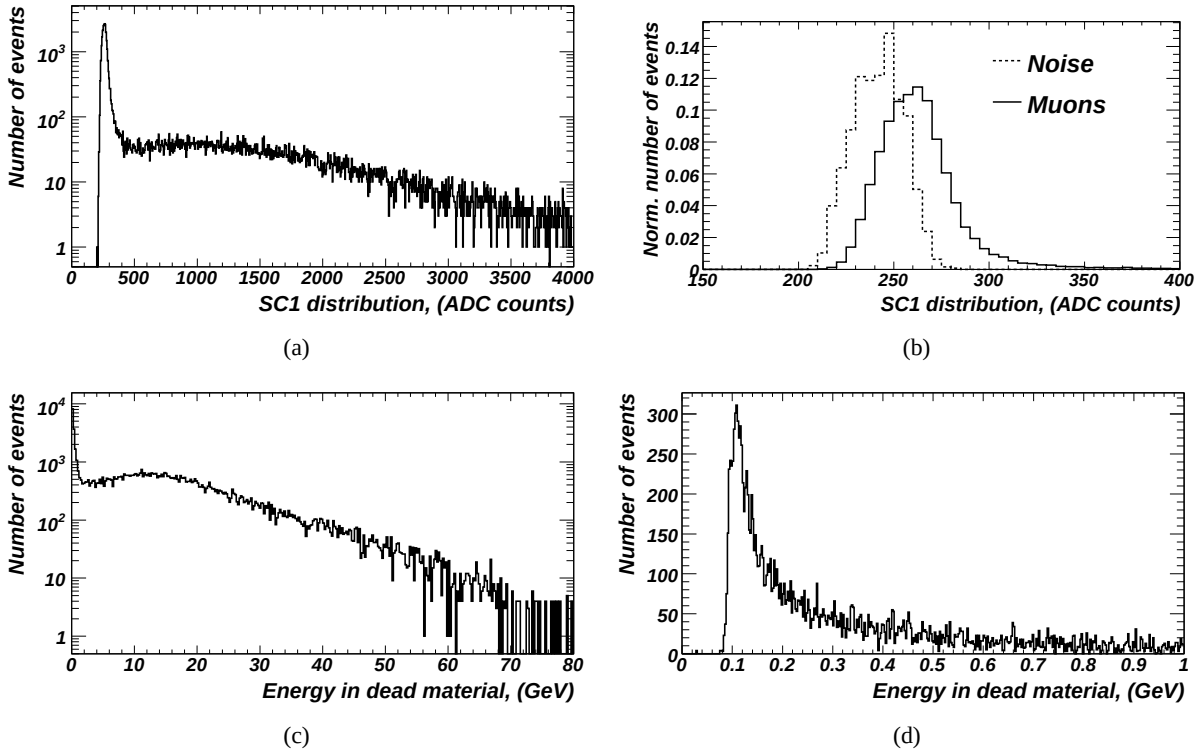

Figure 8: Examples of the measured distributions in the cryostat scintillator (SC1) (in ADC counts) from: a) all particles, b) muons (solid) and randomly triggered noise events (dashed). c) Example distribution for the energy loss in the dead material between the LAr and the Tile calorimeter in simulated events (in GeV) for pions. A magnified view of the small region of the low energy distribution for pions is shown in b) and d). The beam energy is 180 GeV.

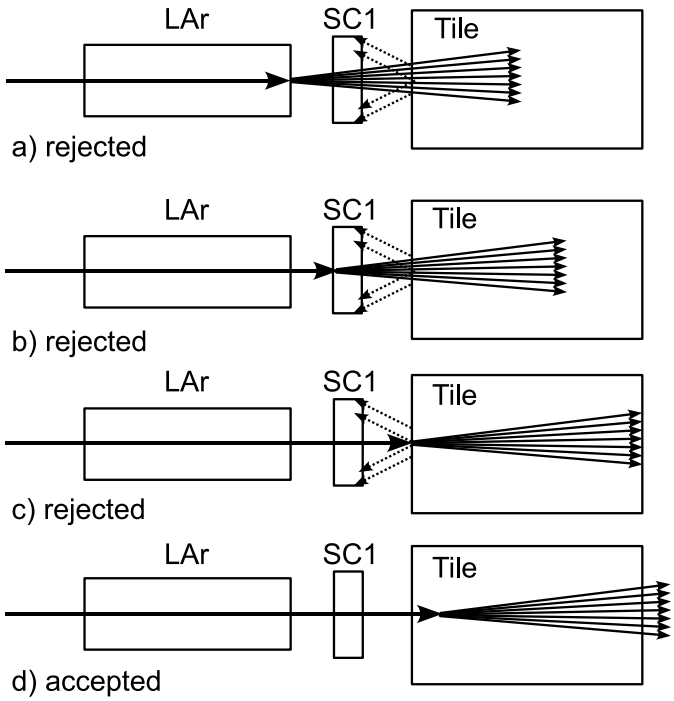

Figure 9: Sketch of various possibilities for the hadron shower development between the LAr and the Tile calorimeter to illustrate the effect of the SC1 cut on the pion response. Backscattering of particles in showers from the first layer of TileCal is indicated by dashed lines. c) and d) illustrate how backscattering (dotted arrows) can effectively change the calorimeter length and increase the longitudinal leakage.

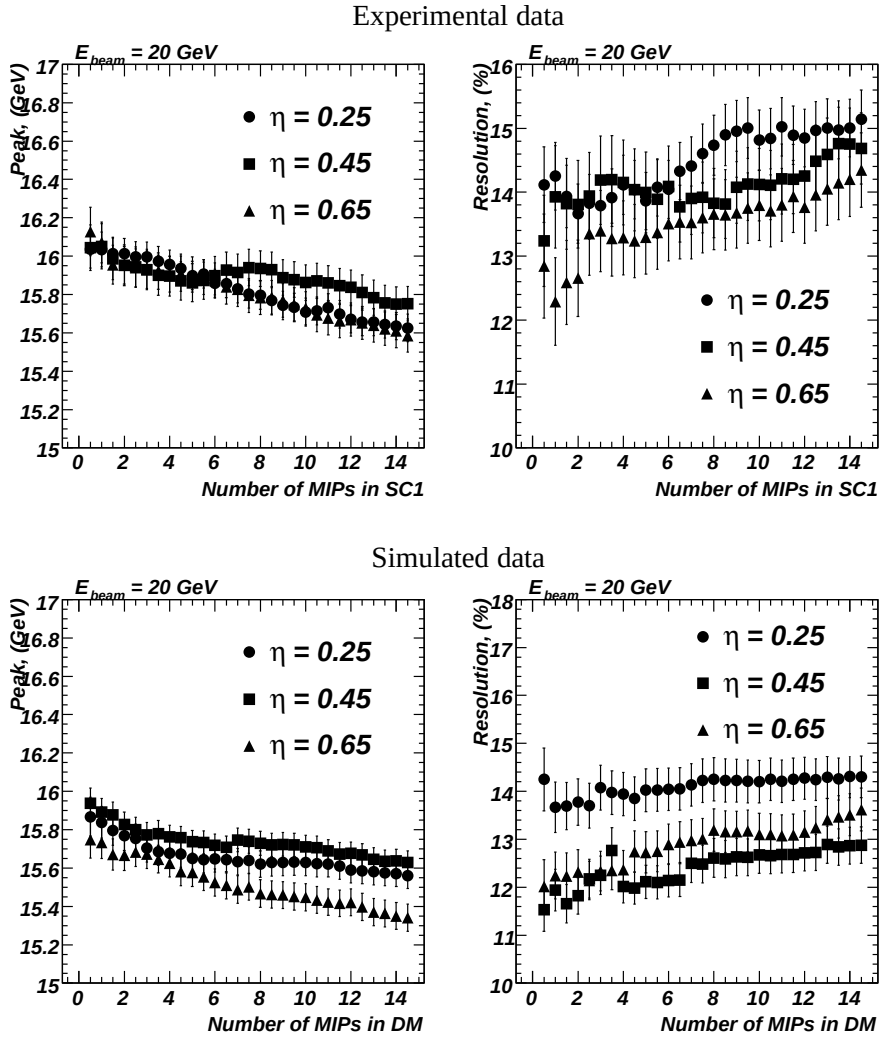

Figure 10: The Tile calorimeter response (left) and resolution (right) measured in test-beam data (top) and Monte Carlo simulations (bottom) for pions with an energy of 20 GeV and a beam impact point of $\eta = 0.25$, 0.45 and 0.65 as a function of a cut on the energy deposited in the SC1 scintillator placed in between the LAr electromagnetic and Tile hadronic calorimeters The cryostat scintillator signal in the data and the total dead material losses in the Monte Carlo simulation is expressed in units equivalent to the energy deposited by a MIP particle.

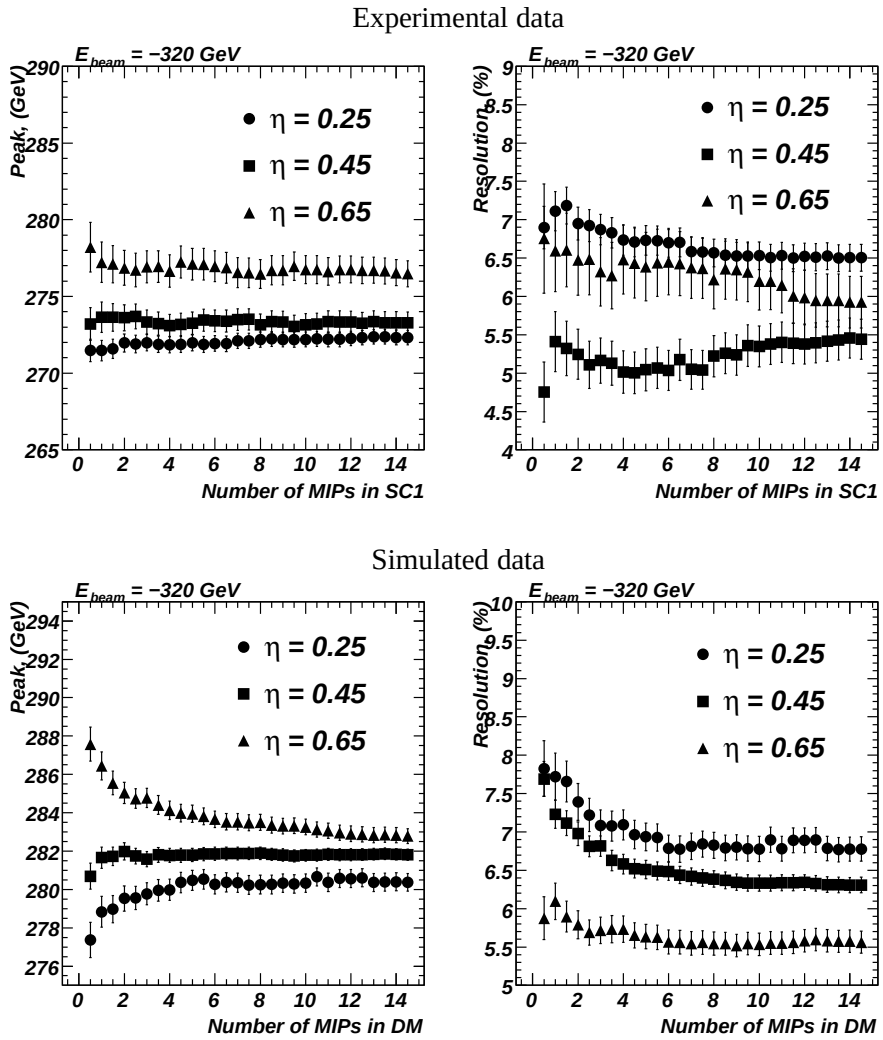

Figure 11: The Tile calorimeter response (left) and resolution (right) measured in test-beam data (top) and Monte Carlo simulation (bottom) for pions with an energy of 320 GeV at beam impact points of $\eta = 0.25$, 0.45 and 0.65 as a function of a cut on the energy deposited in the SC1 scintillator placed in between the LAr electromagnetic and Tile hadronic calorimeters The SC1 signal is calibrated to energy deposited by MIP particles.

Experimental data: 350 and 20 GeV pions $\eta = 0.35$

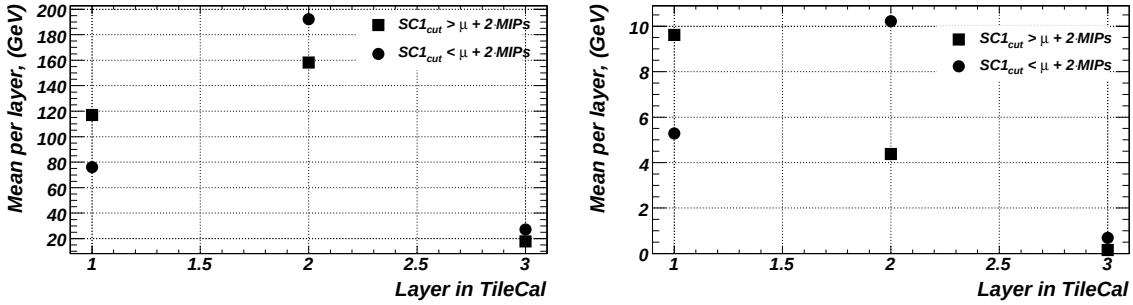

(a) (b)

Monte Carlo simulations: 350 and 20 GeV pions at $\eta = 0.35$

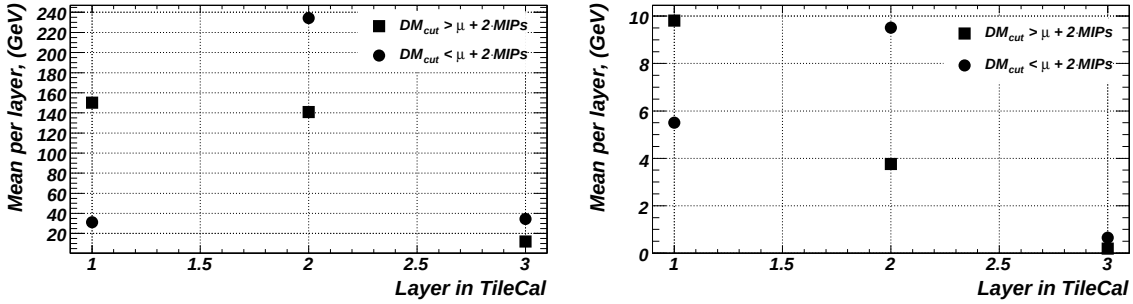

(c) (d)

Figure 12: Mean energy per calorimeter layer (data) as a function of the longitudinal layer in each longitudinal layer for pions with 350 GeV (a) and 20 GeV (b) impinging at $\eta = 0.35$. Event are selected where the deposited energy in the scintillator (SC1) is large or small. The Monte Carlo simulation is shown in c and d.

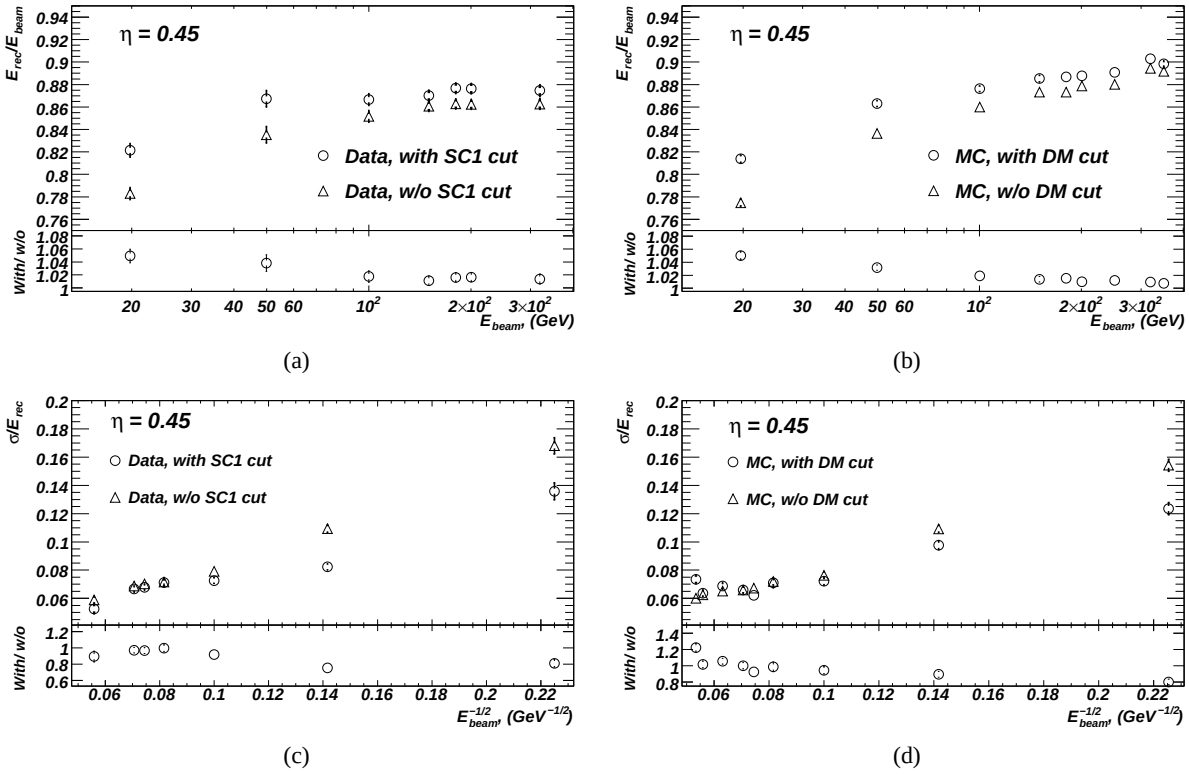

(a) (b)

(c) (d)

Figure 13: Fractional pion response (a,b) and fractional energy resolution (c, d) as a function of the pion beam energy at $\eta = 0.45$ for data (a,c) and Monte Carlo simulations (b,d). Events are selected where a a MIP in electromagnetic LAr calorimeter is imposed (open triangles) and in addition a MIP in the cryostat scintillator (open circles). In the lower plot of the figure the ratio with and without applying a cut on SC1 (DM) is shown.

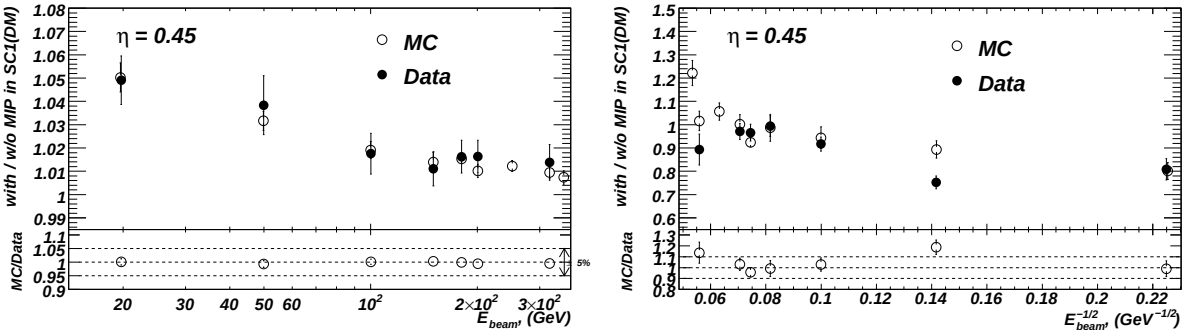

(a) (b)

Figure 14: The ratio of the pion response response (a) and the resolution (b) with and without a MIP cut on the SC1 for pions at $\eta = 0.45$ as a function of the beam energy. Data are shown as closed symbols, Monte Carlo simulation as open symbols. The data to Monte Carlo ratio is shown at the bottom of each figure.

for pion with low and high energy. The Monte Carlo simulation is able to reproduce the changes in the mean calorimeter compartment energy.

Fig. 13 shows the effect of applying a cut on the cryostat scintillator in data and Monte Carlo simulation on the pion response and the resolution at $\eta = 0.45$. for low pion energy a response increase of up to 6% is observed, while for high pion energies the increase is only about 1%. The pion response is unaffected for high pion energies, while it improves by about 20%, if the MIP cut is applied.

Fig. 14 shows that the Monte Carlo simulation is able to reproduce the dependence on the cryostat scintillator cut as observed in the data. The ratio of the reconstructed pion energy with and without this cut as a function of the beam energy for pion impinging at $\eta = 0.45$ is reproduced with 1.2%. The pion energy resolution is reproduced with $10-20$%.

To summarise, for low pion energies energy losses in the dead material due to early starting showers are dominant. Additional losses due to backscattering of hadronic shower particles are less important. For high pion energies losses due the longitudinal leakage are dominant and are increased by requiring small energy in the cryostat scintillator. The energy and pseudo-rapidity dependence of the energy losses is well reproduced by the Monte Carlo simulation.

To reduce efficiently the dead material losses in the analysis the MIP in the SC1 (DM) is imposed for high and low pion energies. We assign a systematic uncertainty of 1.2% on the reconstructed pion energy.

6.4 Longitudinal Leakage Correction

The determinations of the pion response and the resolution are affected by the finite depth of the calorimeter. In particular for high pion energies part of the energy is not contained in the TileCal calorimeter.

The fraction of the energy lost downstream depends on the calorimeter length (usually expressed in interaction lengths λ) that the shower crosses. It therefore varies as a function of the beam impact point.

The energy lost downstream can be obtained using TileCal data collected with the beam hitting the calorimeter from the side (at an angle of 90°) [28] (see Fig 3). This configuration allows full shower containment and makes it possible to measure the deposited energy in different calorimeter volumes up to a depth of 20λ. For each considered calorimeter length a Gaussian fit within $\pm 2\sigma$ is used to determine the peak position. In the case of pion impinging projectively as in the ATLAS configuration the effective detector depth depends on beam impact point η, for example, at $\eta = 0.45$ it is equal to 165 cm.

The peak shift due to longitudinal leakage can be parametrised using the function:

$$A_2 \times exp(-x/B_2), \tag{21}$$

where x is a calorimeter length in cm (see Fig. 15a) The adjusted parameters are given in Table 20.

Using this parametrisation the energy leakage for different beam impact points (in η) can be calculated as a function of the beam energy (see Fig. 15b). A parameterisation for the dependence of the peak leakage on the beam energy can then be obtained using the function:

$$A_3 \cdot (E_{beam})^{B_3}. \tag{22}$$

The values of the parameters are given in Table 21.

The dependence of the TileCal energy resolution on the depth of the calorimeter was studied in a similar way as the response. The depth dependence of the TileCal energy resolution is shown in Fig. 16a for pions as a function of the calorimeter length. The dependence of the energy resolution on the calorimeter length can be parameterised using the function:

$$A_4 \cdot exp(-x/B_4) + C_4, \tag{23}$$

where x is a calorimeter length in cm. The first term of this function describes the variation of the resolution with the calorimeter depth while the second term corresponds to the resolution of a calorimeter at infinite length. The free parameter are again adjusted on the data, where the beam enters TileCal from the side. The obtained values are given in Table 22.

Using these parameterisations correction factors for the TileCal resolution at beam energies of 20, 50, 100 and 180 GeV can be calculated. They are shown in Fig. 16b. The correction to the resolution for a given calorimeter depth with respect to a calorimeter with infinite length as a function of the beam energy is parameterised as

$$A_5 \cdot (E_{beam} + B_5)^{C_5} \tag{24}$$

The obtained parameters are shown in Table 23. The correction factors for the resolution vary from 2.1% at $\eta = 0.65$ and $E_{\text{beam}} = 20$ GeV to 61.5% at $\eta = 0.20$ and $E_{\text{beam}} = 350$ GeV (see Table 19).

The corrections used for the response and the resolution are summarised in Table 18 and in Table 19. The longitudinal leakage corrections for the TileCal response and resolution will be applied in the following analysis.

6.5 Transverse Leakage

The transverse leakage can be estimated in a set-up where five prototype TileCal modules were mounted in a test-beam in the year 1995 [30]. Assuming that the energy of the hadronic shower is contained in five TileCal modules the transverse leakage can be measured by the difference between the mean energy deposited in the three modules to the mean energy reconstructed five modules. The mean energy is calculated from a Gaussian fit to the energy distribution and the peak value is quoted. Fig. 17 shows the obtained transverse leakage as a function of the beam energy. The transverse leakage is about 1.6% at 20 GeV and 0.45% at 300 GeV.

In the following correction for transverse leakage will be applied to the TileCal response.

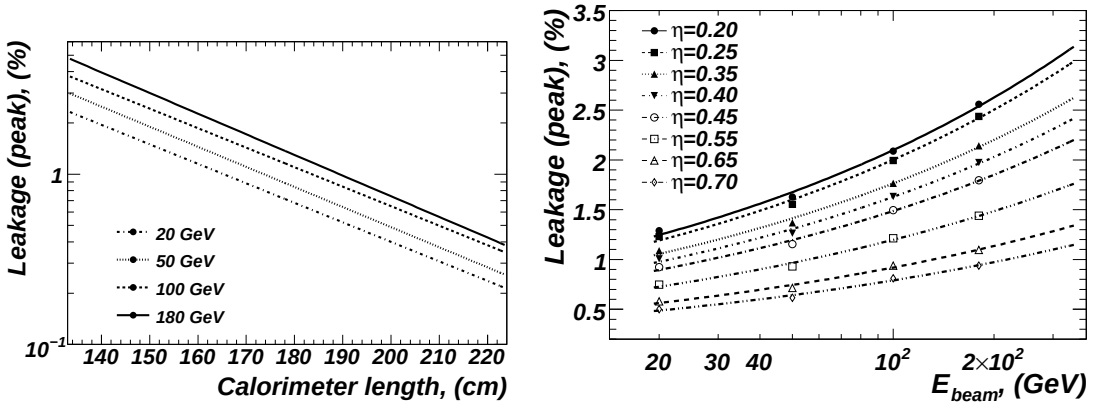

(a) (b)

Figure 15: Parameterisations of the calculated longitudinal peak energy leakage fraction for pions with energies of 20, 50, 100 and 180 GeV as a function of the calorimeter length (a) and as function of the beam energy for various beam impact points. The peak energy is determined by a Gaussian fit within the range of $\pm 2\sigma$.

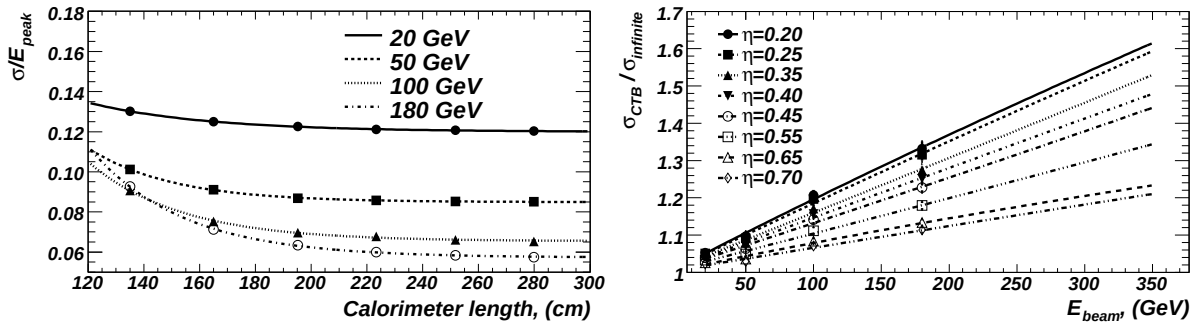

(a) (b)

Figure 16: a) The TileCal energy resolution as a function of the calorimeter length for various beam energies. The solid line denotes a parameterisation corresponding to eq. 23; b) Ratio of the resolution for the TileCal in the CTB set-up with respect to a Tile calorimeter with infinite length as a function of beam energy for various beam impact points η. The solid lines denotes a parameterisation described by eq. 24.

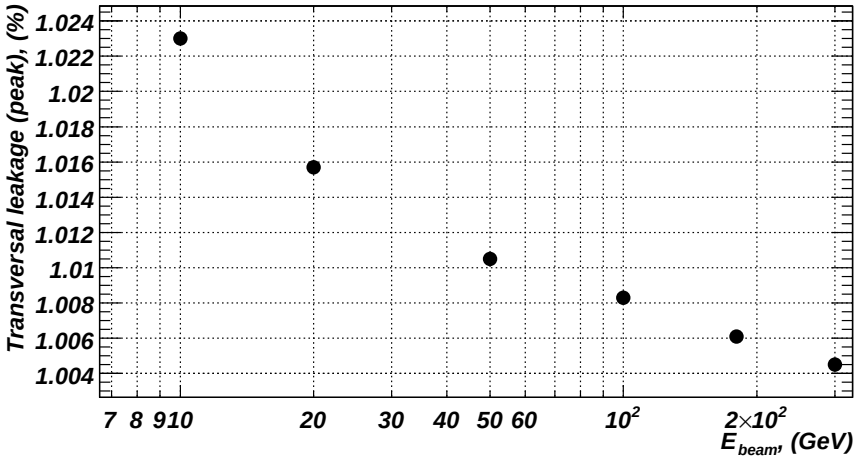

Figure 17: Relative transverse leakage obtained from a fit of the energy distribution measured in three TileCal modules to the one measured in five modules as a function of the beam energy.

7 Measurements of the Energy Response Ratio and of the Fractional Resolution

The pion response has been measured for data and simulated pion samples at various energies and beam impact points. The data were selected by applying the cuts 5 to 12 (see section 4.2). The cuts 7, 9, 11 and 12 were applied to the simulated data.

Corrections for the longitudinal and transversal leakage are applied for data and Monte Carlo simulations. Corrections for the proton contamination are only applied to the data.

7.1 Definition the Fractional Response and Resolution

The energy deposited in TileCal is obtained as the sum of the energies in all PMTs of all three modules using only PMTs with $|E_{\rm PMT}| > 2\sigma_{\rm noise}$. Only PMTs from the C-side ($\eta > 0$) of TileCal modules were considered. The values of the PMT electronic noises, σ_{noise}, is obtained for each PMT for the given run number individually and is measured using random triggers. If the run data has no information about random trigger the σ_{noise} is assumed to be equal to an average value of the PMT noise of 20 MeV for all PMTs. Since, the signal in the PMTs is given in pC, the signal-to-energy conversion factor 1.049 pC/GeV defines the electromagnetic energy scale for data [14].

The reconstructed total energy distribution was fitted by a Gauss function with iteration of the fit in the range of $\pm 2\sigma$ around the mean value. The peak of the energy distribution is quoted as the measurement.

The fractional energy response is defined as:

$$\frac{E_{\pi}^{cor}}{E_{beam} - E_{lost}}, \tag{25}$$

where E_{π}^{cor} is the mean reconstructed pion energy corrected as described in section 6. The variable E_{beam} denotes the beam energy determined using beam line magnets (see Table 26) and E_{lost} is the mean energy lost by pions before reaching the Tile calorimeter. The energy lost before the calorimeter is obtained from a Monte Carlo simulation program (see Fig. 4). The total deposited energy (including the nuclear invisible energy deposits) is quoted.

The fractional resolutions is defined as:

$$\frac{\sigma_\pi^{\rm cor}}{E_\pi^{\rm cor}}, \tag{26}$$

where $\sigma_\pi^{\rm cor}$ is obtained correcting the measured values of σ_π for leakage effects.

As previously discussed correction for the proton contamination and longitudinal leakage are applied both to the mean energy and the energy resolution.

7.2 Systematic Uncertainties

The following systematic uncertainty on the energy measurement have been considered:

- **Charge Injection System (CIS)**. Uncertainties in the electronic calibration introduce an uncertainty on the mean pion energy response (see ref. [12]) as a function of the reconstructed energy (in ADC counts)[6)] that is shown in Fig. 22.
- **Proton contamination correction**. The uncertainties of the ratios of pion to proton response and resolution, and in the parametrisation of the proton fraction in the pion beam were taken into account for the calculation of the proton contamination correction uncertainty.
- **Longitudinal leakage correction** For the longitudinal leakage correction the uncertainty of the parametrisation functions of ratios of responses and resolutions with respect to the responses and resolutions at infinite length were considered.
- **MIP in the SC1 (DM)**. The systematic uncertainty of the MIP cut in the SC1 is $\pm 1.2\%$ for the response and $\pm 10\%$ for the resolution.

The obtained uncertainties for the response and resolution due to the proton contamination and longitudinal leakage corrections are given in Table 5 and Table 6.

	Beam energy (GeV)				
	20	50	100	150	180
Δf_p, (%)	3.6	4.4	5.6	6.4	6.8
$\Delta E_{\rm tot}^{\pi}/E_{\rm tot}^{p})$	0.057	0.042	0.030	0.024	0.022
Δk_p	0.0026	0.014	0.017	0.017	0.017
$\Delta(\sigma_{\rm tot}^{\pi}/\sigma_{\rm tot}^{p})$	0.040	0.039	0.038	0.036	0.036
Δk_p^{σ}	0.0015	0.006	0.009	0.011	0.012

Table 5: Uncertainty on the proton fraction Δf_p in the positively charged pion beam, on the pion to proton response $\Delta(E_{tot}^{\pi}/E_{tot}^{p})$ and on the resolution variation for pion and protons $\Delta(\sigma_{tot}^{\pi}/\sigma_{tot}^{p})$, on proton contamination response correction factors Δk_p and on the proton contamination resolution correction Δk_p^{σ}.

7.3 Results and Data Monte Carlo Comparison

The fractional response of the Tile calorimeter for beam impact points from $\eta = 0.2$ to $\eta = 0.65$ is shown in Fig. 19 for data and Monte Carlo simulation. Statistical and systematic uncertainties are included.

[6)] In ref. [12] the uncertainty on the energy measurement for pions is estimated in low gain only. In order to be able to use these results in high gain, we convert the measured energy to ADC-count using $f_{\rm pC/ADC} = 81.31$ for high gain and $f_{\rm pC/ADC} = 1.294$ for low gain. This is justified, since the non-linearity in the CIS system, only depends on the ADC-counts.

	Leakage uncertainty, (%)											
	Peak						Resolution					
$E_{\text{beam}}^{\text{nom}}$ (GeV)	0.20	0.25	0.35	0.45	0.55	0.65	0.20	0.25	0.35	0.45	0.55	0.65
20	0.17	0.17	0.15	0.13	0.12	0.12	9.6	9.5	9.3	8.5	7.3	9.7
50	0.26	0.25	0.22	0.20	0.18	0.18	10.0	9.9	9.5	8.7	7.4	9.8
100	0.35	0.34	0.30	0.27	0.24	0.24	10.6	10.4	10.0	9.1	7.6	9.9
150	0.42	0.40	0.36	0.32	0.29	0.29	11.1	10.9	10.4	9.4	7.8	10.0
180	0.46	0.43	0.39	0.35	0.32	0.32	11.5	11.2	10.7	9.6	8.0	10.04
200	0.48	0.46	0.41	0.36	0.33	0.33	11.7	11.5	10.8	9.7	8.1	10.08
250	0.53	0.50	0.45	0.40	0.36	0.37	12.3	12.0	11.3	10.1	8.3	10.2
320	0.58	0.56	0.50	0.44	0.41	0.41	13.1	12.8	11.9	10.6	8.6	10.4
350	0.6	0.57	0.52	0.46	0.42	0.43	13.5	13.1	12.2	10.8	8.7	10.5

Table 6: Uncertainty of the longitudinal leakage correction (peak and resolution) at various beam energies E_{beam} and beam impact points η.

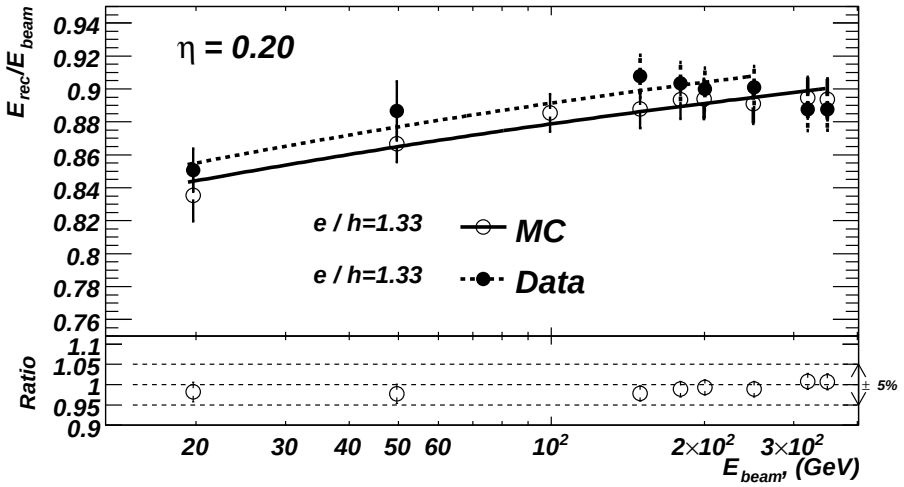

Figure 18: Data to Monte Carlo comparison for the response after having removed the LAr support structure as a function of the beam energy for pions at $\eta = 0.20$.

The response logarithmically increasing towards increases beam energies. This can be interpreted as an increasing fraction of electromagnetic energy towards increasing energy. The measurements for the highest pion energies seems to be lower by about $2-3\%$. This is discussed in more detail in section 10.

Fig. 20 shows the relative pion response as a function of the beam impact points for beam energies from 20 to 350 GeV. For all beam energies the response does not vary with the beam impact point. The rms of the corrected repsonse measurements at a beam energy of 180 GeV is 0.7%. This corresponds approximately to the expected uncertainty due to the non-uniformity of the Tile calorimeter.

The Monte Carlo simulation describes the data within a few percent. Only for the beam impact point at $\eta = 0.2$ the deviation is up to 5%. At this beam impact point there is an additional structure supporting the LAr calorimeter. It is likely that the exact position of this structure is not correctly modelled in the simulation. When the LAr support structure is removed from the simulation, a better agreement of the simulation with the data is found (see Fig. 18).

Fig. 21 shows the resolution as a function of the the inverse square root of the beam energy for beam impact points from $\eta = 0.2$ to $\eta = 0.65$. For high pion energy the resolution is about 5%, while for low

energies it degrades to about 12%. The Monte Carlo simulation is able to describe the data within 10%.

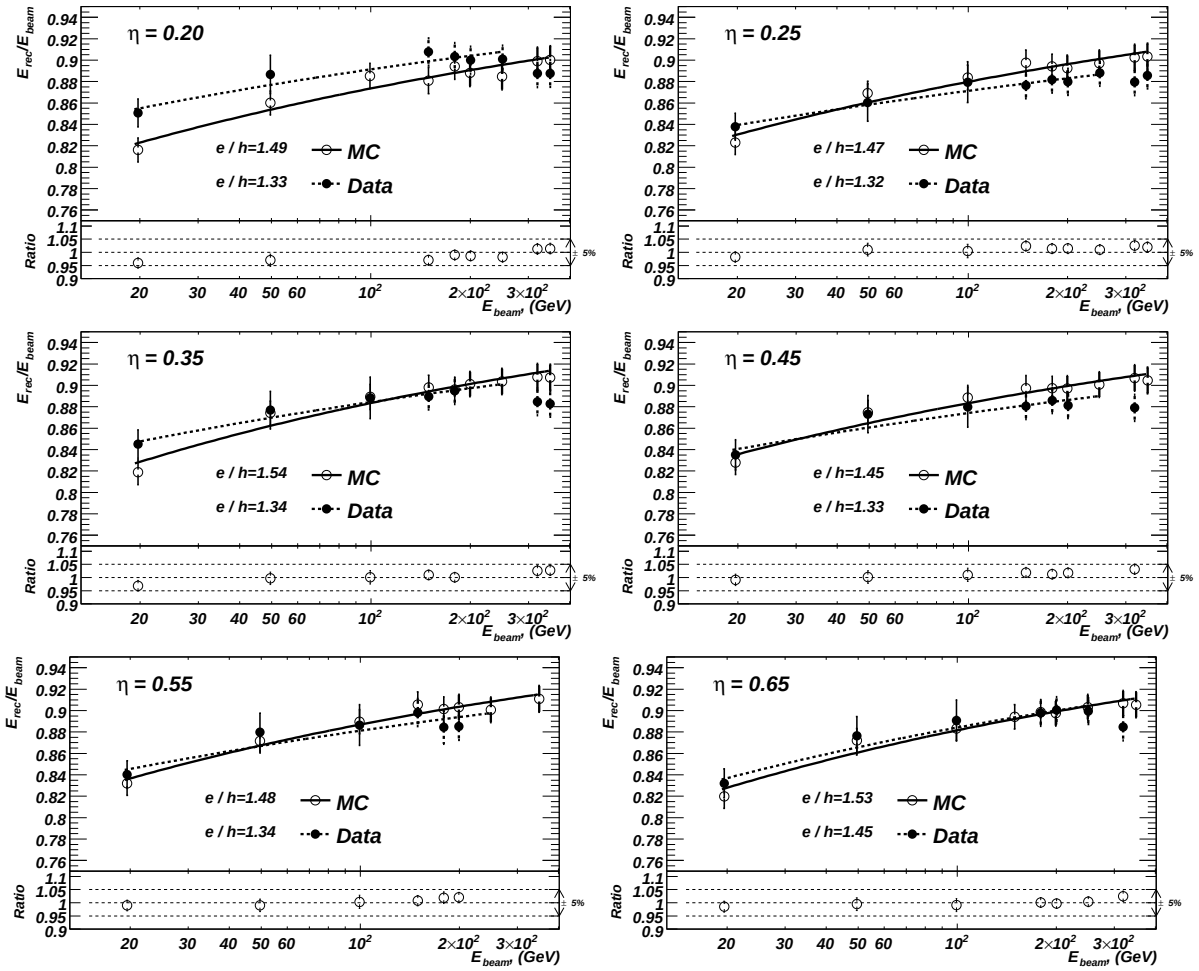

Figure 19: Response of the TileCal as a function of the pion beam energy at various beam impact points η. All corrections are applied. Shown are data (full circles) and Monte Carlo simulations (open circles). Overlayed are the fits of Groom's parametrisation to the data (see text). The error bars include statistical and systematic uncertainties.

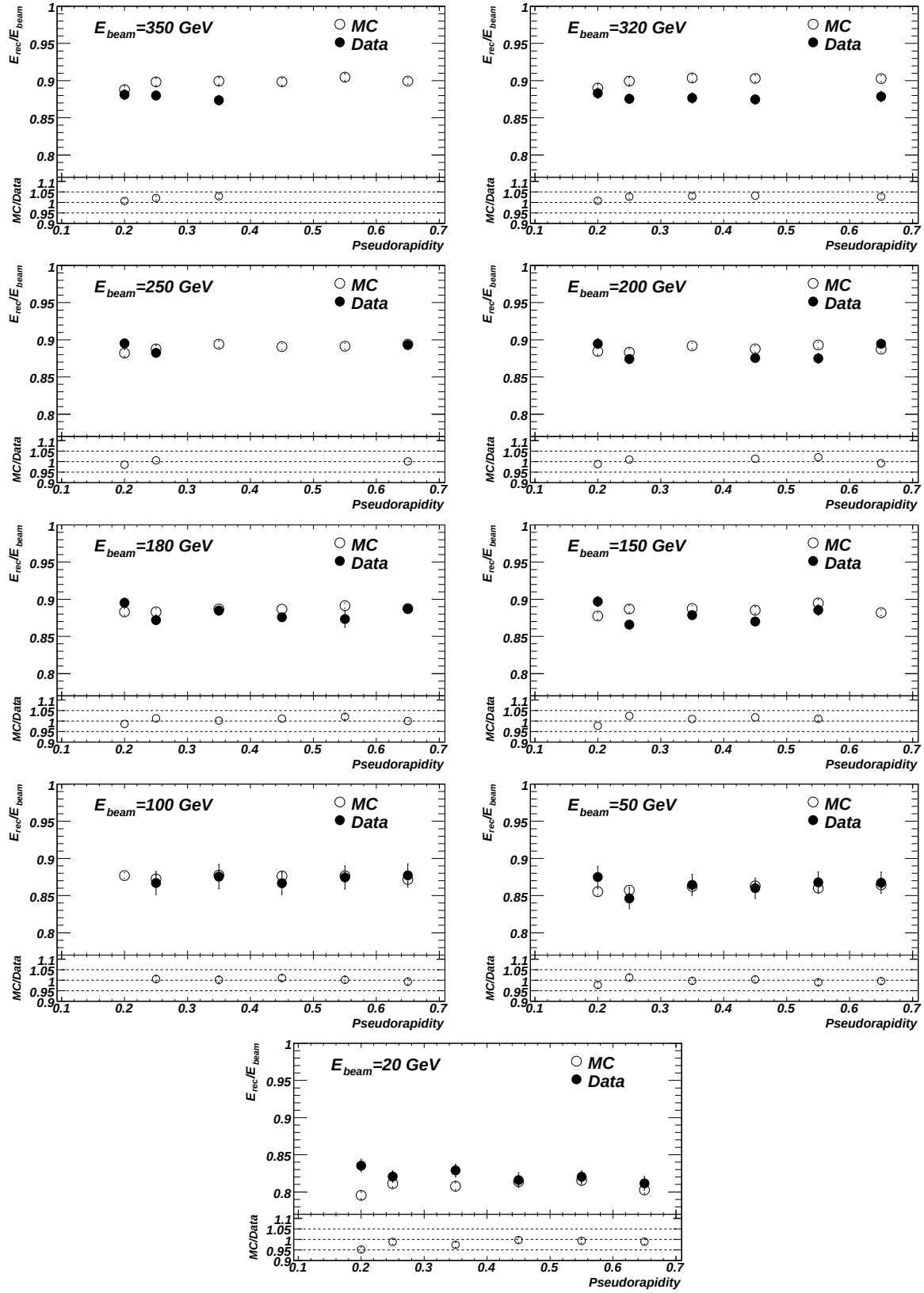

Figure 20: Relative pion response after all corrections as a function of the beam impact point η for beam energies from 20 to 350 GeV. Shown are data (closed circles) and Monte Carlo simulations. The ratio of Monte Carlo simulations to data is included in the bottom of each figure. Both statistical and systematic uncertainties are shown.

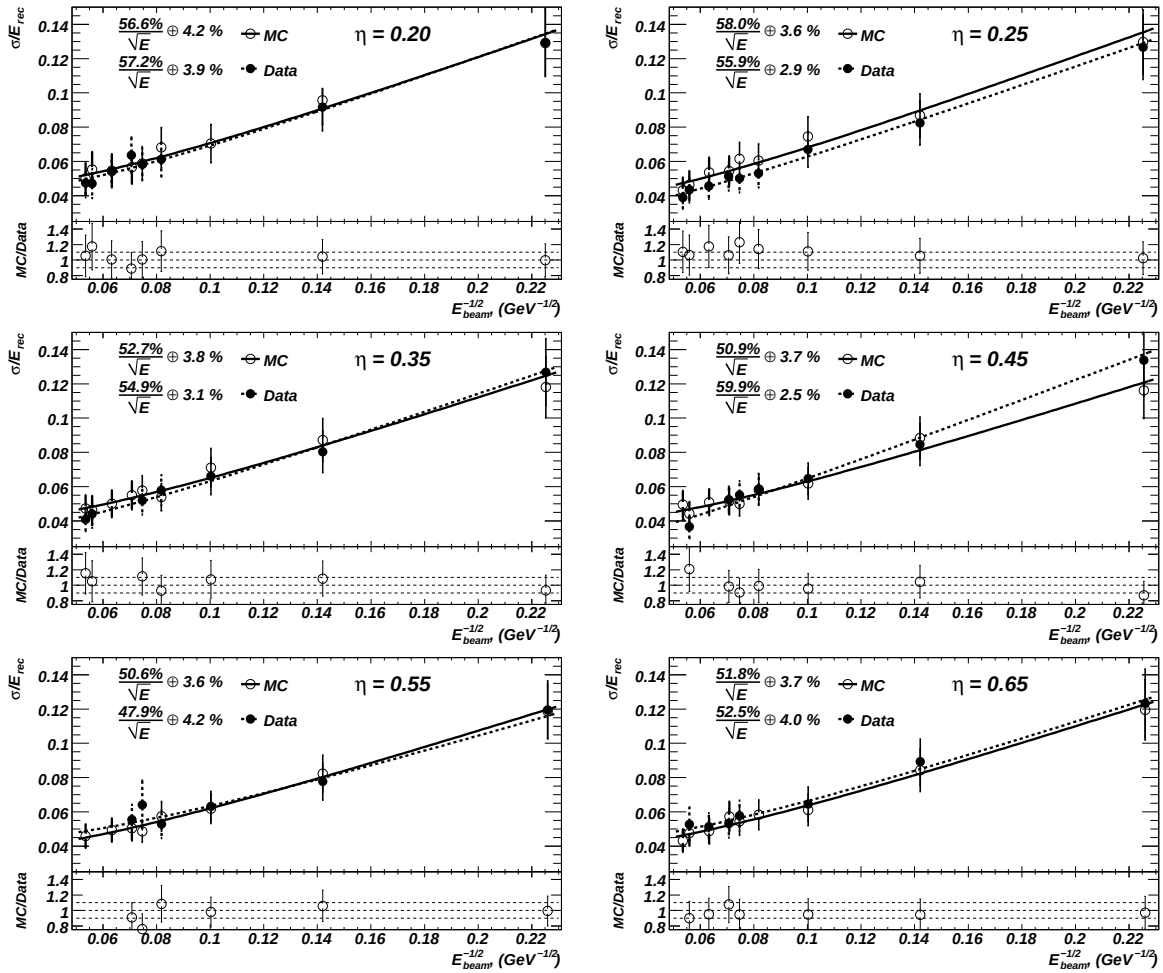

Figure 21: Energy resolution of the TileCal as a function of the pion beam energy at various beam impact points η. All corrections are applied. Shown are data (full circles) and Monte Carlo simulations (open circles). Overlayed is a parameterisation of the dependence of the resolution on the beam energy. The error bars include statistical and systematic uncertainties.

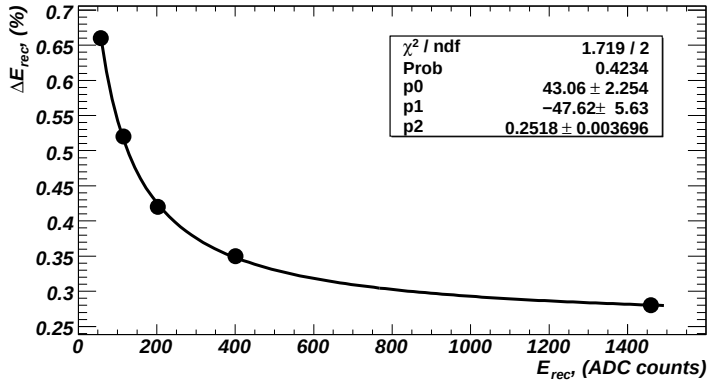

Figure 22: Systematic uncertainty on the energy response introduced by uncertainties in the electronic calibration as a function of the reconstructed pion energy. Overlayed is a parameterisation using the function $p_0/(E_{\mathrm{rec}} - p_1) + p_2$.

8 Phenomenological Interpretation

8.1 Determination of the Hadronic Response Parameters

The measurements of the pion response can be used to extract the response ratio of the calorimeter to purely hadronic and electromagnetic energy depositions.

Following the parameterisation of Groom et al. [31, 32], the non-electromagnetic energy content of hadronic showers induced by incident hadrons of energy E_{beam} can be written as:

$$F_h = \left(\frac{E_{\mathrm{beam}}}{E_0}\right)^{m-1}. \tag{27}$$

The parameter E_0 can be interpreted as the extrapolated energy at which the cascade is entirely hadronic, or an effective turn-on energy for π^0 production. The power m is connected to the mean number of secondaries and the mean energy fraction going to neutral pions in any given strong interaction in the cascade.

The fractional pion response then reads:

$$\frac{E_\pi}{E_{beam}} = (1 - F_h) + F_h \times \left(\frac{e}{h}\right)^{-1}, \tag{28}$$

where E_0, m and e/h are free parameters that are adjusted to the data.

The parameterisation eq. 28 successfully describes various measurements of many calorimeters [31, 32].

For the adjustment of the free parameters to data, the first parameter is fixed to $E_0 = 1$ GeV and the parameters m and e/h are fitted. The obtained fits are superimposed to the data in Fig. 19. The values of m and e/h are reported in Table 7 for the data and the MC simulation. The quoted uncertainties include the statistical and the systematics uncertainties.

The parameter m is on average determined to be $m = 0.83 \pm 0.02$. The variation with the beam impact point is small. The values found with the Monte Carlo simulation are a bit smaller: $m = 0.78 \pm 0.01$.

The e/h parameter is found to be on average $e/h = 1.35 \pm 0.04$. The dependence of the beam impact point is small. The Monte Carlo simulation predicts a larger value $e/h = 1.49 \pm 0.04$. Note, that the parameter m and e/h are correlated in the fit.

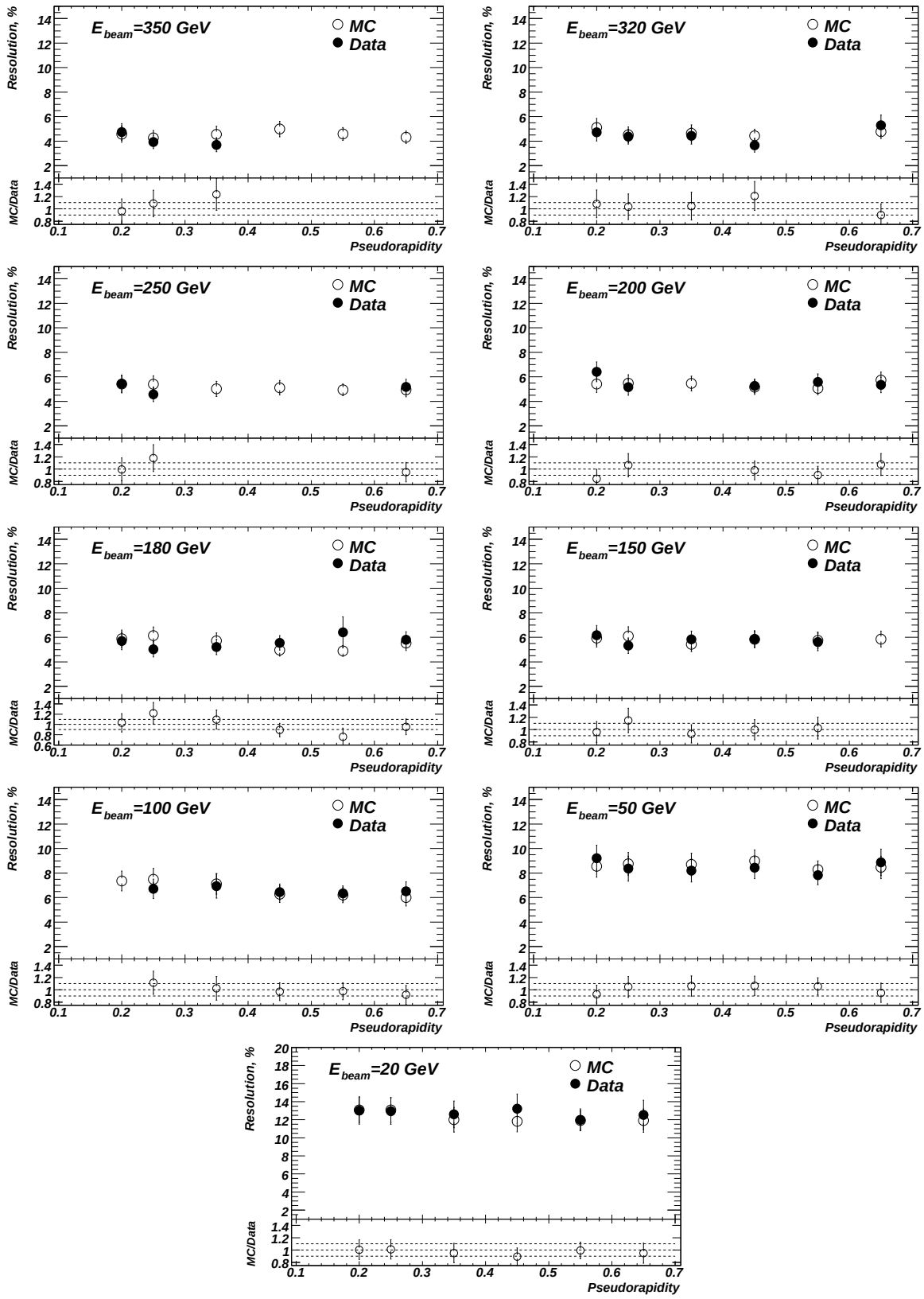

Figure 23: Pion energy resolution after all corrections as a function of the beam impact point η for beam energies from 20 to 350 GeV. Shown are data (closed circles) and Monte Carlo simulations. The ratio of Monte Carlo simulations to data is included in the bottom of each figure. Both statistical and systematic uncertainties are shown.

	Test-beam data		Simulation	
η	m	e/h	m	e/h
0.20	0.82±0.049	1.33±0.097	0.79±0.032	1.49±0.053
0.25	0.86±0.040	1.32±0.078	0.79±0.033	1.47±0.105
0.35	0.83±0.056	1.34±0.108	0.76±0.034	1.54±0.113
0.45	0.85±0.048	1.33±0.095	0.79±0.033	1.45±0.100
0.55	0.84±0.050	1.34±0.098	0.77±0.036	1.48±0.114
0.65	0.79±0.046	1.45±0.131	0.77±0.032	1.53±0.118
Average	0.83±0.020	1.35±0.042	0.78±0.014	1.49±0.042

Table 7: Fitted values for the pion response parameters m and e/h obtained using Groom's parameterisation for the electromagnetic energy fraction (eq. 28). The results are given for data and Monte Carlo simulations at various beam impact points η.

8.2 Parametrisation of the Resolution

The measurements of the resolution can be used to extract the resolution sampling and the constant term for the various beam impact points. The following parameterisation is adjusted to the data:

$$\frac{\sigma_{\text{rec}}}{E_{\text{rec}}} = \frac{a}{\sqrt{E_{\text{beam}}}} \oplus b. \tag{29}$$

The parameter a characterises the sampling fluctuations and the parameter b represents the constant term, i.e. it describes the calorimeter resolution at very large pion energies.

The results of the fit is shown in Fig 21. The experimental resolutions are well represented by the parameterisation. The values of a, b obtained in a fit to the data are reported in Table 8.

In the data, the average sampling term is found to be $a = 54.7 \pm 3$ and the constant term 3.4%. The result obtained for the Monte Carlo simulation are compatible.

	Test-beam data		Simulation	
η	a (%)	b (%)	a (%)	b (%)
0.20	57.2±7.9	3.9±0.8	56.6±7.7	4.2±0.8
0.25	55.9±6.7	2.9±0.8	58.0±7.1	3.6±0.8
0.35	54.9±6.9	3.1±0.8	52.7±7.0	3.8±0.7
0.45	59.9±7.2	2.5±1.2	50.9±6.4	3.7±0.6
0.55	47.9±7.6	4.2±1.0	50.6±6.2	3.6±0.6
0.65	52.5±8.0	4.0±0.8	51.8±6.7	3.7±0.6
Average	54.7±3.0	3.4±0.37	53.4±2.8	3.8±0.28

Table 8: Parameters a and b describing the calorimeter resolution for data and Monte Carlo simulations at various beam impact points. The calorimeter resolution is corrected for longitudinal leakage effects.

9 Comparison with Previous Results

The results obtained in the combined test-beam 2004 for the events where pions shower only in the TileCal can be compared to earlier measurement where only the TileCal was exposed to a pion test-beam.

Results for pions with a beam impact point of $\eta = 0.35$ are compared to measurements from the 2002 test-beam [13] where 11% of the TileCal production modules were tested and from the 1995 test-beam

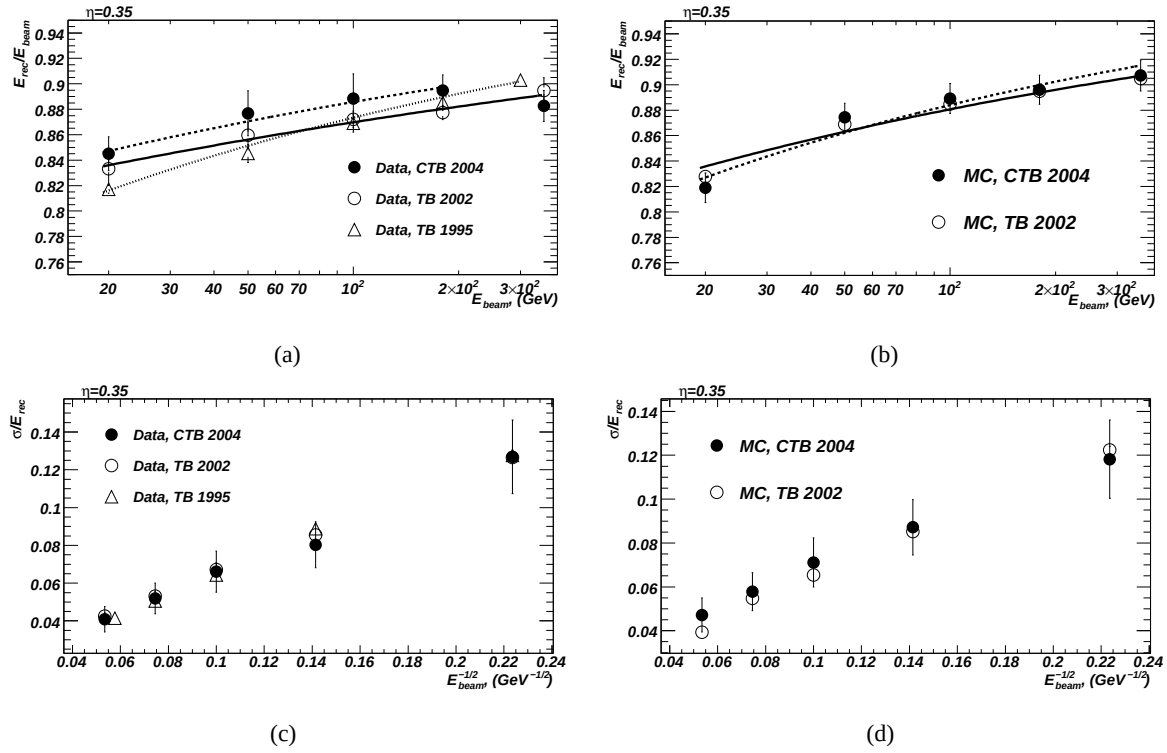

Figure 24: Response (a,b) and resolution (c,d) for pions in the test-beams of the year 1995 and 2002 and the 2004 combined test-beam as a function of the beam energy for pions at $\eta = 0.35$: Data (a,c) as well as Monte Carlo simulations (b,d) are shown. Corrections for proton contamination and longitudinal leakage were applied. For the test-beam data taken in 1995 and 2002 uncertainties due to the correction for proton contamination or longitudinal leakage are not included.

[30] where proto-type modules were used. The prototype modules used in 1995 had a more granular cell segmentation and were also a bit longer.

The response and the resolution for both 1995 and 2002 test-beam data are corrected for longitudinal leakage. In the 2002 test-beam analysis a clean sample of pions was selected using a Cerenkov detector in the beam-line. For the 1995 results a correction for proton contamination has been applied. Systematic uncertainties of proton contamination and longitudinal leakage corrections for test-beam 1995 and 2002 data were not considered.

Fig. 24a shows the pion response as a function of the pion beam energy obtained in the test-beam data taken in 1995 and 2002 and in this analysis (CTB 2004). Table 9 presents the pion response for each of the considered test-beam measurement. The response in the combined test-beam 2004 is systematically higher than in the previous test-beam by about 2% with respect to the 2002 test-beam and by about $2-4\%$ to the 1995 test-beam. The data from 2004 and 2002 are in agreement within the systematic uncertainty. the higher response in the 1995 data might be explained by the missing correction for proton contamintation. The response expected from the Monte Carlo simulation agree with 1%.

Table 11 shows the fit results for Groom's parameterisation (eq. 27 and eq. 28). Similar results are obtained for the hadronic response parameter e/h for the test-beam 2002 and 2004 data. In test-beam 1995 the e/h value is a bit higher, but also the m parameter is lower. Since these two parameters are correlated, the difference in the single parameter appear to be larger than the differences in the data.

	Test-beam data				
	2002	1995	2004	2004/2002	2004/1995
20	0.833±0.012	0.817±0.005	0.845±0.013	1.014	1.034
50	0.860±0.011	0.845±0.003	0.877±0.018	1.020	1.038
100	0.872±0.007	0.869±0.007	0.888±0.020	1.018	1.022
180	0.877±0.006	0.885±0.010	0.895±0.012	1.021	1.011
300	–	0.903±0.002	–	–	–
350	0.895±0.010	–	0.883±0.012	0.987	–

	Simulation		
	2002	2004	2004/2002
20	0.828±0.002	0.819±0.012	0.989
50	0.869±0.002	0.874±0.011	1.006
100	0.885±0.001	0.889±0.012	1.005
180	0.895±0.001	0.896±0.011	1.001
350	0.905±0.001	0.907±0.012	1.002

Table 9: Pion response ($E_{\mathrm{rec}}/E_{\mathrm{beam}}$) in test-beam data measured in the years 1995, 2002 and the CTB 2004 and Monte Carlo simulations. For the test-beam data taken in 1995 and 2002 uncertainties due to the correction for proton contamination or longitudinal leakage are not included.

	Test-beam data				
	2002	1995	2004	2004/2002	2004/1995
20	12.66±0.26	12.76±0.21	12.68±1.95	1.002	0.994
50	8.56±0.15	8.88±0.12	8.03±1.21	0.938	0.904
100	6.72±0.36	6.43±0.08	6.61±1.09	0.984	1.028
180	5.32±0.26	5.05±0.06	5.19±0.8	0.976	1.028
300	–	4.15±0.05	–	–	–
350	4.25±0.19	–	4.09±0.7	0.962	–

	Simulation		
	2002	2004	2004/2002
20	12.24±1.79	11.82±1.79	0.966
50	8.52±1.26	8.72±1.26	1.024
100	6.54±1.11	7.11±1.11	1.087
180	5.47±0.86	5.78±0.86	1.057
350	3.93±0.10	4.72±0.78	1.20

Table 10: Energy resolution (σ/E_{rec} (in percent) for test-beam taken in the years 1995, 2002 and the CTB 2004 and for Monte Carlo simulations. For the test-beam data taken in 1995 and 2002 uncertainties due to the corrections for proton contamination or longitudinal leakage are not included.

	Test-beam data			Simulation	
	2002	1995	2004	2002	2004
e/h	1.34±0.07	1.58±0.04	1.36±0.13	1.42±0.01	1.57±0.16
m	0.86±0.03	0.77±0.01	0.82±0.07	0.80±0.04	0.75±0.04

Table 11: Response parameter m and e/h parameters obtained with Groom's parameterisation form data of test-beams in the years 2002, 1995 and the CTB 2004 and their Monte Carlo simulations.

10 Discussion of the Results at 320 and 350 GeV

The measurements presented in the previous section for very high pion energies, i.e. 320 and 350 GeV, appear to be a bit lower than expected by the Monte Carlo simulations as well as by the logarithmic increase of the pion response as a function of the beam energies. The apparent drop is about $2-3\%$, but is observed for all beam impact points where high energy data are available. In the following possible reasons for the energy drop are discussed.

For technical reasons the SPS beams at very high energy are shifted vertically with respect to the nominal beam axis. This might influence the TileCal response. The lateral leakage might be increased or the response might be changed because of cell inhomogeneities.

The beam shift with respect to the nominal beam axis can be measured with the TileCal by studying the asymmetry between the energy depositions in the top (C_2) and the bottom module (C_0). If the beam hits the TileCal in the centre, the asymmetry is expected to be zero.

The top-bottom asymmetry can be defined either using the total energy deposited in the top and bottom modules or using the two PMTs in the central module:

$$\frac{E(C_2)-E(C_0)}{E(C_2)+E(C_0)} \quad \text{and} \quad \frac{E(C_1^{\text{Up}})-E(C_1^{\text{Down}})}{E(C_1^{\text{Up}})+E(C_1^{\text{Down}})}, \tag{30}$$

where $E(C_0)$ and $E(C_2)$ is the mean total energy deposited in bottom and top modules and $E(C_1^{\text{Up}})$ and $E(C_1^{\text{Down}})$ is the energy deposited in top and bottom PMTs of the central module (C_1).

Fig. 25a shows the asymmetry for the two definitions as a function of the beam energy. While the beam is well centred for low pion energies, for energies beyond 200 GeV an increasing asymmetry for increasing beam energies is observed. At 350 GeV the asymmetry reaches of $\sim 24\%$ for the top-bottom module asymmetry and $\sim 6\%$ for PMT up-down asymmetry.

The shift in the beam position can also be observed in the LAr calorimeter. Using the azimuthal angle corresponding to the barycentre of the cluster in the second layer of the LAr calorimeter together with the known inner radius of the middle layer ($R_2^{LAr} = 1750$ mm), the mean impact point can be calculated. Only clusters with $E_{\text{clust}} > 2$ GeV and close to the nominal beam impact point ($|\Delta\phi| < 0.1$) are considered.

The calculated impact point as a function of the beam momentum at $\eta = 0.35$ is shown in Fig. 25b. The same trend as for the top-bottom asymmetry in the TileCal is observed. From 200 GeV onwards the asymmetry increases towards increasing energy. At the highest energy the beam is shifted by $20-30$ mm.

The influence of the shifted beam position on the lateral leakage can be tested with a Monte Carlo simulation. Monte Carlo simulation samples with a beam shifted by 20 and 40 mm for $E_{beam} = 320$ and 350 GeV at $\eta = 0.35$ are compared to the default simulation with no beam shift (see Fig. 26). The influence of 20 mm shift is negligibly small. A 40 mm beam shift decreases the response by $0.2-0.3\%$.

Even though it is known that the Monte Carlo simulation produces hadronic showers that are narrower than the ones in the data it is unlikely that the observed reduction of the pion response by $2-3\%$ can be explained by lateral leakage.

Other effects caused by the beam shift are still under consideration.

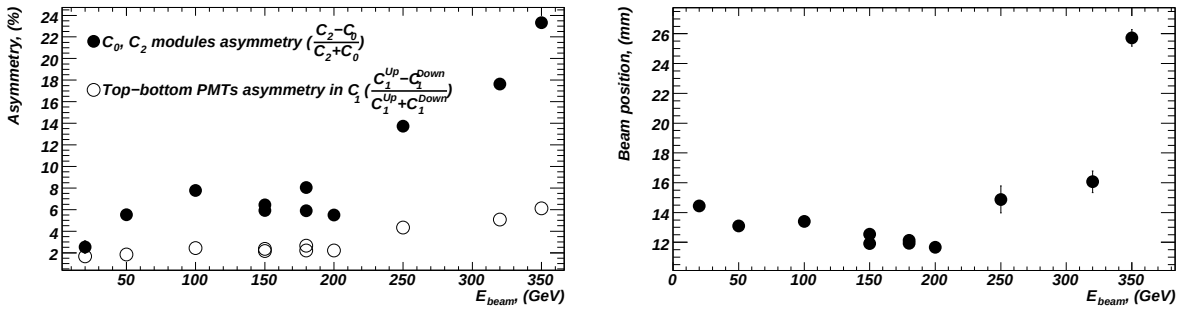

(a) (b)

Figure 25: a) Top-bottom module asymmetry (closed circles) and top-bottom PMT asymmetry (open circles) and b) beam impact point calculated using the clusters coordinates of the middle layer of LAr calorimeter as a function of the beam energy. The beam impact point is $\eta = 0.35$. Only statistical uncertainties are shown.

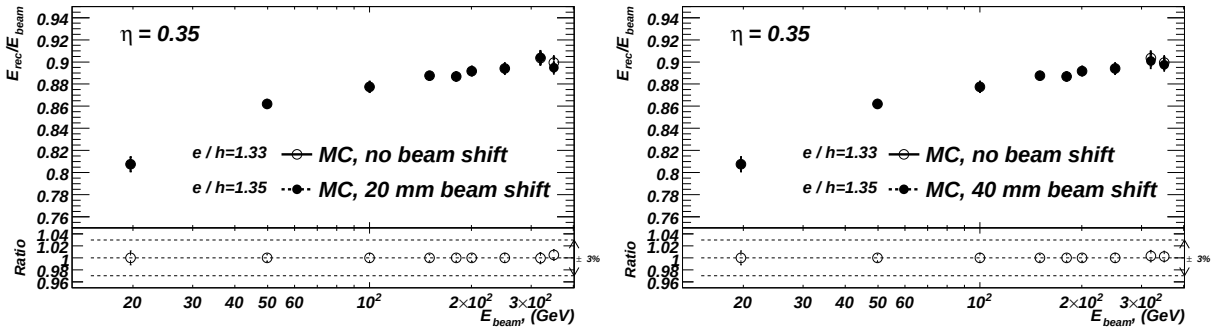

Figure 26: Influence of the beam impact point shift on the response for the pion energies of 320 and 350 GeV at $\eta = 0.35$ a) for a 20 mm shift and b) for a 40 mm beam shift for a Monte Carlo simulation. Statistical and systematic uncertainties are shown.

Conclusion

The response and resolution of pions has been studied in the combined test-beam data taken in the year 2004, where a slice of the ATLAS detector was placed in the CERN SPS H8 beam-line. Pions showering in the Tile calorimeter have been selected. Measurements have been made for pions from 20 to 350 GeV and for beam impact points from $0.2 \leq \eta \leq 0.65$.

The results have been corrected for proton contamination and longitudinal leakage. Possible biases due to the selection procedure of events where pions pass a minimally ionising particles before entering the Tile calorimeter have been carefully evaluated.

The pion response increases logarithmically towards higher energies as expected from the increasing amount of electromagnetic energy in the hadron shower development. For the highest measured beam energy a decrease with respect to this expectation has been observed. The reason for this decrease is still unclear.

Using Groom's parameterisation the hadronic response is $e/h = 1.35$ and the energy fraction going into charged pions is $m = 0.83$. The energy resolution is $\sigma/E = (54.7 \pm 3.0)\%/\sqrt{E} \oplus (3.4 \pm 0.37)\%$. Note, that here the energy resolution has been corrected for longitudinal leaakage. No strong dependence on the beam impact point is found.

These results are compatible to earlier measurements in 1995 and 2002 test-beams where only the Tile calorimeter had been exposed to pion beams. However, in the earlier measurement no decrease at high energies had been observed.

The Monte Carlo describes the pion response in the data within a few percent and the energy resolution within 10%.

References

[1] S.Gadomski et al., ATL-COM-DAQ-2005-014 (2005).

[2] S. Agostinelli et al., Nucl. Instrum. Meth. **A 506** (2003) 250.

[3] J. Spanggaard, Internal report, CERN SL-Note 98-023-BI.

[4] B. Girolamo et al., Beamline instrumentation in the 2004 combined ATLAS testbeam, Internal Report ATLAS-TECH-PUB-2005-001, CERN, Geneva, Switzerland, 2005.

[5] ATLAS Collaboration, Inner detector Technical Design Report, Internal Report 1997, CERN, Geneva, Switzerland, CERN/LHCC 97-16, Volume II CERN/LHCC 97-17.

[6] ATLAS Collaboration, Technical Design Report, Internal Report May, Technical Design Report of the Lar Calorimeter, 1999.

[7] ATLAS collaboration, CERN/LHCC/96-42 (CERN, Geneva (Switzerland) 1996).

[8] ATLAS Collaboration, Muon spectrometer Technical Design Report, Internal report, CERN, Geneva, Switzerland, CERN/LHCC 97-022.

[9] M. Aharrouche et al., Nucl. Instrum. Meth. **A 568** (2006) 601–623.

[10] M. Aleksa et al., ATLAS Combined Testbeam: Computation and Validation of the Electronic Calibration Constants for the Electromagnetic Calorimeter, Internal Report CERN, Genva, ATL-LARG-PUB-2006-003, Apr 2006.

[11] W. E. Cleland and E. G. Stern, Nucl. Instrum. Meth. **A 338** (1994) 467.

[12] M. Hurwitz et al., Performance and Calibration of the TileCal Fast Readout Using the Charge Injection System, Internal Report ATL-COM-TILECAL-2008-003, CERN, 2008.

[13] P. Amaral et al., ATL-TILECAL-PUB-2009-002; ATL-COM-TILECAL-2009-004, CERN, Geneva (Switzerland) submitted to Nucl. Instrum. Meth. (2009).

[14] K.J. Anderson et al., Calibration of ATLAS Tile Calorimeter at Electromagnetic Scale, Internal Report CERN, Geneva, Switzerland, ATL-COM-TILECAL-2008-016, CERN, November 2008.

[15] G. Folger and J.-P. Wellisch, Proceedings of International conference on: Computing in High Energy Physics ,La Jolla (California) **nucl-th/0306007** (2003).

[16] N. S. Amelin et al., Phys. Rev. Lett. **67** (1991) 1523.

[17] N. S. Amelin et al., Nucl. Phys. **A 544** (1992) 463.

[18] L. V. Bravina et al., Nucl. Phys. **A 566** (1994) 461.

[19] L. V. Bravina et al., Phys. Lett. **B 344** (1995) 49.

[20] M. P. Guthrie, R. G. Alsmiller and H. W. Bertini, Nucl. Instr. and Meth. **66** (1968) 29.

[21] H. W. Bertini and P. Guthrie, Nucl. Instr. and Meth. **A 169** (1971) 670.

[22] N. V. Stepanov, ITEP Preprint ITEP-55 (Moscow) (1988).

[23] J. B. Birks, Phys. Rev. **86** (1952) 569.

[24] J. B. Birks, New York, Pergamon Press (1964).

[25] R. L. Craun and D. L. Smith, Nucl. Instr. and Meth. **80** (1970) 239.

[26] F. Spano, Simulation of the full noise pattern in Tile Calorimeter Front End electronics : a phenomenological approach to coherent effects, Internal Report ATL-COM-TILECAL-2008-009, CERN, Jul 2008.

[27] G. Aad et al., JINST **3 S08003** (2008).

[28] H. Hakobyan, M. Simonyan, T. Carli and A. Henriques, ATL-TILECAL-PUB-2007-00, CERN, Geneva (Switzerland) (2007).

[29] S. Constantinescu et al., ATL-TILECAL-2001-005, CERN, Geneva (Switzerland) (2001).

[30] T. Davidek, M. Volpi, T. Zenis, in preparation (2009).

[31] T. A. Gabriel et al., Nucl. Instrum. Meth. **A 338** (1994) 336.

[32] D. E. Groom, Nucl. Instrum. Meth. **A 572** (2007) 628 and erratum ibid A 503 (2008) 628.

	Test-beam data			Simulation			MC/Data	
$E_{\mathrm{beam}}^{\mathrm{nominal}}$ (GeV)	Peak (GeV)	σ (GeV)	σ/Peak (%)	Peak (GeV)	σ (GeV)	σ/Peak %	Peak	σ/Peak
350	310.04	14.68	4.73	314.50	15.70	4.99	1.01	1.06
320	283.46	13.34	4.71	287.09	15.87	5.53	1.01	1.17
250	225.73	12.23	5.42	220.79	12.03	5.45	0.98	1.01
200	180.49	11.48	6.36	177.23	10.03	5.66	0.99	0.89
180	162.13	9.47	5.84	160.46	9.43	5.87	0.99	1.01
150	135.75	8.30	6.12	131.74	8.97	6.81	0.97	1.11
100	–	–	–	87.98	6.19	7.04	–	–
50	44.05	4.04	9.17	42.73	4.09	9.57	0.97	1.04
20	16.79	2.17	12.94	16.11	2.08	12.91	0.96	1.00

Table 12: Reconstructed pion energy (Peak), standard deviation (σ) and the resolution (Peak/σ) at $\eta = 0.20$ for pions showering in TileCal only. Given are the results in the data and in the Monte Carlo simulation.

	Test-beam data			Simulation			MC/Data	
$E_{\mathrm{beam}}^{\mathrm{nominal}}$ (GeV)	Peak (GeV)	σ (GeV)	σ/Peak (%)	Peak (GeV)	σ (GeV)	σ/Peak (%)	Peak	σ/Peak
350	309.39	12.06	3.90	315.54	13.60	4.31	1.02	1.11
320	280.92	12.22	4.35	288.18	13.36	4.63	1.03	1.07
250	222.44	10.13	4.56	223.81	12.00	5.36	1.01	1.18
200	176.39	9.05	5.13	178.06	9.69	5.44	1.02	1.06
180	158.28	7.92	5.01	160.51	9.88	6.16	1.01	1.23
150	131.03	6.95	5.30	134.2	8.12	6.05	1.02	1.14
100	87.58	5.87	6.70	88.01	6.56	7.45	1.01	1.11
50	42.70	3.52	8.24	43.13	3.74	8.68	1.01	1.05
20	16.52	2.09	12.67	16.22	2.10	12.97	0.98	1.02

Table 13: Reconstructed pion energy (Peak), standard deviation (σ) and the resolution (Peak/σ) at $\eta = 0.25$ for pions showering in TileCal only. Given are the results in the data and in the Monte Carlo simulation.

	Test-beam data			Simulation			MC/Data	
$E_{\text{beam}}^{\text{nominal}}$ (GeV)	Peak (GeV)	σ (GeV)	σ/Peak (%)	Peak (GeV)	σ (GeV)	σ/Peak (%)	Peak	σ/Peak
350	308.29	12.60	4.09	316.88	14.95	4.72	1.03	1.16
320	282.53	12.44	4.40	289.85	13.41	4.63	1.03	1.05
250	–	–	–	225.29	11.27	5.00	–	–
200	–	–	–	179.78	9.87	5.49	–	–
180	160.58	8.33	5.19	160.82	9.30	5.78	1.00	1.11
150	133.00	7.70	5.79	134.28	7.23	5.39	1.01	0.93
100	88.41	5.85	6.61	88.49	6.29	7.11	1.00	1.08
50	43.49	3.49	8.03	43.37	3.78	8.72	1.00	1.09
20	16.66	2.11	12.68	16.14	1.91	11.82	0.97	0.93

Table 14: Reconstructed pion energy (Peak), standard deviation (σ) and the resolution (Peak/σ) at $\eta = 0.35$ for pions showering in TileCal only. Given are the results in the data and in the Monte Carlo simulation.

	Test-beam data			Simulation			MC/Data	
$E_{\text{beam}}^{\text{nominal}}$ (GeV)	Peak (GeV)	σ (GeV)	σ/Peak (%)	Peak (GeV)	σ (GeV)	σ/Peak (%)	Peak	σ/Peak
350	–	–	–	315.99	15.67	4.96	–	–
320	280.60	10.26	3.66	289.51	12.79	4.42	1.03	1.21
250	–	–	–	224.53	11.42	5.09	–	–
200	176.62	9.25	5.24	178.90	9.22	5.16	1.02	0.98
180	158.96	8.76	5.51	161.00	8.04	4.99	1.01	0.91
150	131.60	7.72	5.87	134.11	7.79	5.81	1.02	0.99
100	87.53	5.66	6.46	88.41	5.47	6.18	1.01	0.96
50	43.30	3.66	8.46	43.38	3.84	8.84	1.00	1.05
20	16.42	2.20	13.38	16.27	1.89	11.61	0.99	0.87

Table 15: Reconstructed pion energy (Peak), standard deviation (σ) and the resolution (Peak/σ) at $\eta = 0.45$ for pions showering in TileCal only. Given are the results in the data and in the Monte Carlo simulation.

	Test-beam data			Simulation			MC/Data	
$E_{\mathrm{beam}}^{\mathrm{nominal}}$ (GeV)	Peak (GeV)	σ (GeV)	σ/Peak (%)	Peak (GeV)	σ (GeV)	σ/Peak (%)	Peak	σ/Peak
350	–	–	–	318.10	14.58	4.58	–	–
320	–	–	–	–	–	–	–	–
250	–	–	–	224.54	11.08	4.94	–	–
200	176.48	9.78	5.54	180.08	9.07	5.04	1.02	0.91
180	158.65	10.16	6.41	161.67	7.87	4.87	1.02	0.76
150	134.18	7.09	5.29	135.28	7.76	5.74	1.01	1.09
100	88.19	5.58	6.32	88.50	5.48	6.19	1.00	0.98
50	43.64	3.39	7.77	43.22	3.56	8.23	0.99	1.06
20	16.46	1.97	11.96	16.29	1.94	11.88	0.99	0.99

Table 16: Reconstructed pion energy (Peak), standard deviation (σ) and the resolution (Peak/σ) at $\eta = 0.55$ for pions showering in TileCal only. Given are the results in the data and in the Monte Carlo simulation.

	Test-beam data			Simulation			MC/Data	
$E_{\mathrm{beam}}^{\mathrm{nominal}}$ (GeV)	Peak (GeV)	σ (GeV)	σ/Peak (%)	Peak (GeV)	σ (GeV)	σ/Peak (%)	Peak	σ/Peak
350	–	–	–	316.19	13.66	4.32	–	–
320	282.39	14.89	5.27	289.39	13.74	4.75	1.03	0.90
250	225.10	11.55	5.13	225.13	10.99	4.88	1.00	0.95
200	180.39	9.60	5.32	178.89	10.25	5.73	1.00	1.08
180	161.00	9.29	5.77	161.11	8.78	5.45	1.00	0.95
150	–	–	–	133.54	7.78	5.83	–	–
100	88.55	5.72	6.46	87.80	5.37	6.11	0.99	0.95
50	43.39	3.88	8.94	43.17	3.64	8.43	1.00	0.94
20	16.29	2.01	12.33	16.05	1.92	11.96	0.99	0.97

Table 17: Reconstructed pion energy (Peak), standard deviation (σ) and the resolution (Peak/σ) at $\eta = 0.65$ for pions showering in TileCal only. Given are the results in the data and in the Monte Carlo simulation.

	Leakage (peak) (%)					
$E_{\text{beam}}^{\text{nom}}$ (GeV)	0.20	0.25	0.35	0.45	0.55	0.65
20	1.25	1.19	1.06	0.90	0.73	0.56
50	1.68	1.60	1.41	1.19	0.97	0.75
100	2.10	2.00	1.76	1.49	1.20	0.92
150	2.39	2.28	2.01	1.69	1.36	1.04
180	2.54	2.42	2.13	1.79	1.44	1.10
200	2.63	2.50	2.20	1.85	1.49	1.14
250	2.82	2.69	2.36	1.99	1.59	1.22
320	3.06	2.91	2.56	2.15	1.72	1.31
350	3.15	2.99	2.63	2.21	1.77	1.35

Table 18: Fraction of the energy lost (in percent) by longitudinal leakage (peak) for various beam energies E_{beam} and beam impact points η.

	Leakage (resolution) (%)					
$E_{\text{beam}}^{\text{nom}}$ (GeV)	0.20	0.25	0.35	0.45	0.55	0.65
20	5.1	4.9	4.3	3.7	2.9	2.1
50	10.6	10.0	8.7	7.2	5.7	4.3
100	19.6	18.5	16.0	13.2	10.4	7.9
150	28.4	26.9	23.3	19.3	15.1	11.3
180	33.5	31.9	27.8	23.0	18.0	13.2
200	36.9	35.2	30.7	25.4	20.0	14.5
250	45.3	43.3	38.1	31.6	24.7	17.6
320	56.7	54.6	48.5	40.4	31.5	21.7
350	61.5	59.4	53.0	44.2	34.4	23.3

Table 19: Correction factors (in percentage) for longitudinal leakage to the energy resolution at various beam energies E_{beam} and beam impact points η.

$E_{\text{beam}}^{\text{nom}}$ (GeV)	A_2 (%)	B_2 (cm)
20	78.4	37.9
50	112	36.8
100	127	37.9
150	–	–
180	198	35.8

Table 20: Parameters of the function eq. 21 correcting the peak energy for longitudinal leakage. The variable *x* denotes the calorimeter length.

	η					
	0.20	0.25	0.35	0.45	0.55	0.65
A_3 (%)	0.4726	0.4532	0.4050	0.3480	0.2870	0.2268
B_3	0.3237	0.3226	0.3195	0.3154	0.3102	0.304

Table 21: Parameters of the function as given by eq. 22 correcting for energy losses due to longitudinal leakage (peak) as a function of the beam energy for various beam impact points η.

$E_{\text{beam}}^{\text{nom}}$ (GeV)	A_4	B_4 (cm)	C_4
20	0.24	42.91	0.120
50	1.44	30.14	0.085
100	1.45	33.33	0.065
180	2.01	33.42	0.057

Table 22: Parameters obtained for eq. 23 correcting the resolution as a function of the TileCal depth.

	η					
	0.20	0.25	0.35	0.45	0.55	0.65
A_5 (%)	0.013	0.006	0.0008	0.00014	0.0002	0.097
B_5	395.1	483.01	755.15	1091.01	1305.03	488.69
C_5	0.735	0.829	1.079	1.27	1.19	0.378

Table 23: Parameters obtained for eq. 24 correcting the resolution for energy lost due to longitudinal leakage for various beam impact points.

Run number	$E_{\text{beam}}^{\text{nom}}$, (GeV)	η	E_{beam}^{meas}, (GeV)	ΔE_{beam}^{meas}, (%)
2100476	20	0.20	20.20	1.34
2100477			–//–	
2100132	50	0.20	50.30	0.71
2100133			–//–	
–	100	0.20	–	–
2100102			150.82	
2100466			150.82	
2100467	150	0.20	150.79	0.53
2100468			150.82	
2100469			150.79	
2100093			–//–	
2100094	180	0.20	180.91	0.52
2100463			–//–	
1002081	-150	0.20	150.76	0.53
1002083			–//–	
1002098			180.89	
1002099			180.89	
1002103	-180	0.20	180.91	0.52
1002104			180.89	
1002105			180.91	
1002106			180.89	
1002132			200.99	
1002135			200.99	
1002139			201.02	
1002141	-200	0.20	200.99	0.52
1002143			200.99	
1002144			200.99	
1002146			201.02	
1002161			251.20	
1002170	-250	0.20	251.22	0.51
1002172			251.20	
1002173			251.20	
2100029	-320	0.20	320.15	0.51
2100028	-350	0.20	350.83	0.51
2100055			–//–	

Run number	$E_{\text{beam}}^{\text{nom}}$, GeV	η	$E_{\text{beam}}^{\text{meas}}$, GeV
2100479			–//–
2100480	20	0.25	20.20
2100481			–//–
2100177	50	0.25	50.30
2100172	100	0.25	100.54
2100173			–//–
2100168			150.82
2100169			150.82
2100170			150.79
2100171	150	0.25	150.82
2100453			150.82
2100454			150.79
2100455			150.79
2100456			150.76
2100161			–//–
2100162			–//–
2100164	180	0.25	180.91
2100460			–//–
2100461			–//–
1003002			–//–
1003007			–//–
1003008	-150	0.25	150.76
1003009			–//–
1003010			–//–
1002214			180.92
1002216			180.91
1002217	-180	0.25	180.91
1002221			180.91
1002223			180.91
1002191			201.00
1002192			200.99
1002193	-200	0.25	201.02
1002194			200.99
1002198			201.00
1002199			201.02
1002174	-250	0.25	251.20
1002175			–//–
2100053	-320	0.25	320.15
2100030			–//–
2100031	-350	0.25	350.83
2100054			350.85

Run number	$E_{\text{beam}}^{\text{nom}}$, GeV	η	$E_{\text{beam}}^{\text{meas}}$, GeV
2100482	20	0.35	20.20
2100492			–//–
2100249	50	0.35	50.30
2100251			–//–
2100349	100	0.35	100.54
2100449			150.82
2100450	150	0.35	150.82
2100451			150.79
2100452			150.79
2100207			180.91
2100209	180	0.35	–//–
2100445			–//–
2100446			–//–
1003012			–//–
1003014			–//–
1003019			–//–
1003020	-150	0.35	150.76
1003021			–//–
1003022			–//–
1003023			–//–
1003037			–//–
1003039			–//–
1003040	-180	0.35	180.91
1003041			–//–
1003042			–//–
1003043			–//–
–	-200	0.35	–
–	-250	0.35	–
2100034	-320	0.35	320.15
2100033	-350	0.35	350.83

Run number	E_{beam}^{nom}, GeV	η	E_{beam}^{meas}, GeV
2100494	20	0.45	20.20
2100498			–//–
2100300			50.30
2100327	50	0.45	–//–
2100328			–//–
2100291			100.54
2100292	100	0.45	–//–
2100325			–//–
2100326			–//–
2100273			150.79
2100274			150.82
2100275	150	0.45	150.82
2100432			150.79
2100433			150.82
2100435			150.82
2100257			180.91
2100267			180.89
2100269	180	0.45	180.91
2100318			180.91
2100443			180.89
2100444			180.91
1002071			–//–
1002072	-150	0.45	150.76
1002073			–//–
1002074			–//–
1002052			180.92
1002053	-180	0.45	180.92
1002054			180.91
1002056			180.91
1002041			–//–
1002042	-200	0.45	201.02
1002043			–//–
1002045			–//–
–	-250	0.45	–
2100051	-320	0.45	320.15
–	-350	0.45	–

Run number	$E_{\text{beam}}^{\text{nom}}$, GeV	η	$E_{\text{beam}}^{\text{meas}}$, GeV
2100501	20	0.55	–//–
2100504			20.20
2100510			–//–
2100359	50	0.55	50.30
2100362			–//–
2100351	100	0.55	100.54
2100352			–//–
2100424	150	0.55	150.82
2100425			150.79
2100426			150.82
2100421	180	0.55	180.91
2100422			180.92
1003150	-150	0.55	–//–
1003151			150.76
1003152			–//–
1003136	-180	0.55	180.89
1003095	-200	0.55	201.02
1003096			201.02
1003098			201.02
1003104			201.00
1003105			201.02
1003106			200.99
1003087	-250	0.55	251.20
1003088			–//–
–	-320	0.55	–
–	-350	0.55	–

Run number	$E_{\text{beam}}^{\text{nom}}$, GeV	η	$E_{\text{beam}}^{\text{meas}}$, GeV
2100513	20	0.65	20.20
2100514			–//–
2100363	50	0.65	50.30
2100364			–//–
2100371			–//–
2100372	100	0.65	100.54
2100373			–//–
2100380			150.79
2100382	150	0.65	150.79
2100383			150.82
2100386			150.82
2100388	180	0.65	180.91
2100389			–//–
–	-150	0.65	–
1003194			180.89
1003195			180.91
1003197	-180	0.65	180.91
1003198			180.89
1003199			180.91
1003200			180.91
1003214			201.02
1003215			201.02
1003216	-200	0.65	200.99
1003217			200.99
1003220			200.99
1003222			200.99
1003241			–//–
1003242			–//–
1003244	-250	0.65	251.20
1003245			–//–
1003246			–//–
2100048	-320	0.65	320.15
–	-350	0.65	–

Table 26: Nominal and measured beam energies, and number of pions and proton contamination for run numbers used for analysis.